Online Range Monitoring in Carbon Ion Radiotherapy using Interaction Vertex Imaging

Doctoral thesis

for

the award of the doctoral degree

of the Faculty of Mathematics and Natural Sciences

of the University of Cologne

submitted by

Devin Hymers

accepted in the year 2025

Abstract

Carbon ion radiotherapy delivers a precise and highly conformal dose distribution, which maximizes dose to the target while minimizing the dose to surrounding healthy tissue, and particularly to radiosensitive organs at risk. However, inherent uncertainties in dose delivery limit the extent to which these advantages may be utilized. Range monitoring methods, such as Interaction Vertex Imaging (IVI), provide feedback on the position of the carbon ion beam within the patient, and have the potential to allow more conformal dose distributions which take full advantage of the sharp dose maximum, or Bragg peak, produced when an ion beam stops inside a patient. The prototype filtered IVI (fIVI) Range Monitoring System is the first device to apply large-area (36 cm^2 and 72 cm^2) silicon sensors to the online monitoring of carbon ion radiotherapy treatments. This system consists of two layers of thin, double-sided strip-segmented silicon detectors, and associated fast readout electronics, to monitor charged particles produced by beam-patient interactions during irradiation. To validate this prototype for the demanding clinical environment, initial commissioning tests were performed using sources and low-energy ion beams. These tests were followed by measurement of clinical beams of varying range in human-sized plastic phantoms, modelling a treatment. In addition to offline analysis, these clinical measurements were saved for real-time playback, to allow assessment of the online acquisition and analysis performance.

This promising system meets and exceeds the demands of clinical irradiation. It is capable of accepting count rates beyond 1.0 MHz with negligible losses due to pileup, and extremely low random coincidence rates. During clinical irradiation of a target representing the human head, Bragg peak depth differences on the order of 1.0 mm could be distinguished; with the collection of additional data modelling a larger full-scale sensor array, sub-millimeter precision is possible. These range differences can consistently be determined less than 200 ms after the end of irradiation, as the majority of data processing occurs concurrently with data collection. This setup extends the millimetric precision achieved by prior IVI studies to the more challenging and clinically important case of shallow Bragg peak positions. The speed of online monitoring is comparable to required beam pauses for a change in energy, making it feasible to detect the presence of a range error and abort irradiation prior to delivery of the next beam in the treatment plan. This combination of fast online analysis and high precision enabled by the fIVI Range Monitoring System provides the potential to shrink margins which account for

dose delivery uncertainty, by providing an additional safety feature in clinical irradiation. This margin reduction would allow further sparing of healthy tissue and limit the risk of complications in carbon ion radiotherapy while maintaining the same rate of treatment success.

Zusammenfassung

Die Kohlenstoffionen-Strahlentherapie liefert eine präzise und hochgradig konforme Dosisverteilung, die die Dosis für das Ziel maximiert und gleichzeitig die Dosis für das umgebende gesunde Gewebe und insbesondere für strahlenempfindliche Risikoorgane minimiert. Allerdings schränken inhärente Unsicherheiten bei der Bestrahlung das Ausmaß ein, in dem diese Vorteile voll genutzt werden können. Methoden zur Überwachung der Reichweite des Strahls, wie das Interaction Vertex Imaging (IVI), erlauben es die Position der Kohlenstoff-Ionen im Patienten zu bestimmen. Somit wird eine gleichmäßigere Dosisverteilung ermöglicht, die das scharfe Dosismaximum, den sogenannten "Bragg-Peak", der entsteht, wenn ein Ionenstrahl im Patienten stoppt, voll ausnutzt. Der in dieser Arbeit entwickelte Prototyp eines Silizium-Trackingdetektors für das "filtered IVI" (fIVI)- ist das erste Gerät welches großflächige ($36\,\mathrm{cm}^2$ und $72\,\mathrm{cm}^2$) Siliziumsensoren für eine Online-Strahlentherapiebehandlung einsetzt. Dieses System besteht aus zwei Schichten dünner, doppelseitiger, streifenförmiger Siliziumdetektoren und zugehöriger schneller Ausleseelektronik, um die geladenen Teilchen zu detektieren, die während der Bestrahlung durch die Wechselwirkung von Strahl und Patient emittiert werden. Um diesen Prototyp für die anspruchsvolle klinische Umgebung zu validieren, wurden erste Tests mit Quellen und Ionenstrahlen niedriger Energie durchgeführt. Anschließend wurden klinische Strahlen unterschiedlicher Reichweite in Kunststoffphantomen mit realistischen klinischen Dimensionen gemessen, die eine Behandlung realistisch simulieren. Zusätzlich zur Offline-Analyse wurden diese klinischen Messungen genutzt, um eine Online-Analyse in Echtzeit zu entwickeln und zu testen.

Das in dieser Arbeit entwickelte System erfüllt und übertrifft die Anforderungen der klinischen Bestrahlung. Es ist in der Lage, Zählraten von über 1.0 MHz mit vernachlässigbaren Verlusten aufgrund von Pile-up und extrem niedrigen Zufallskoinzidenzen zu verarbeiten. Bei der klinischen Bestrahlung eines Ziels, das den menschlichen Kopf repräsentiert, konnten Bragg-Peak-Tiefenunterschiede in der Größenordnung von 1.0 mm festgestellt werden; mit der Erfassung zusätzlicher Daten, die ein größeres Sensorarray modellieren, ist eine Präzision im Submillimeterbereich möglich. Diese Reichweitenunterschiede können in weniger als 200 ms nach dem Ende der jeweiligen Bestrahlung bestimmt werden, da der Großteil der Datenverarbeitung synchron mit der Datenerfassung erfolgt. Mit diesem Aufbau wird die in früheren IVI-Studien erreichte Präzision im Millimeterbereich auf den anspruchsvolleren und klinisch

wichtigen Fall der weniger tiefen Bragg-Peak-Positionen ausgedehnt. Die Geschwindigkeit der Online-Überwachung ist vergleichbar mit den erforderlichen Strahlpausen für eine Energieänderung, so dass es möglich ist, das Vorhandensein eines Bereichsfehlers zu erkennen und die Bestrahlung vor der Abgabe des nächsten Strahls im Behandlungsplan abzubrechen. Diese Kombination aus schneller Online-Analyse und hoher Präzision des Silizium-Trackers bietet das Potenzial das Planungsvolumen möglichst eng an das Zielvolumen zu legen ohne große Sicherheitsmargen einbeziehen zu müssen. Diese Verkleinerung der Margen erlaubt eine Schonung des gesunden Gewebes und damit eine Reduktion der Komplikationen bei der Kohlenstoff-Ionentherapie, ohne hierbei die Erfolgsaussichten der Bestrahlung zu schmälern.

Dedication

For Leo and Lucy, my constant companions.

Acknowledgements

I would like to thank everyone who has encouraged me and cheered me on throughout the past several years. There are too many of you to name, but know that each and every one of you have made a difference, and I could not have made it across this finish line without your support.

This project was funded, in part, through a Canada Graduate Scholarship administered by the Natural Sciences and Engineering Research Council of Canada (NSERC), award ID CGSD3-560138-2021. Thank you to Sherley Montauban, the administrator at NSERC who supported me in changing the location of tenure of this award from Canada to Cologne.

To my family and friends from Canada, thank you for giving me the courage to move across an ocean, learn a new language, explore a new culture, and have an experience unlike anything else. Although I am not usually one to step outside of my comfort zone, I am grateful for the encouragement I needed to seize the incredible opportunity placed before me.

To the Mücher group, and the entire IKP, thank you for accepting me, helping me find my footing, and providing such a positive and supportive working environment. I am deeply grateful to have gotten to know each of you, and I already miss working with you every day. In particular, thank you to Sebastian Schroeder and Laila Weisel, our little medical physics subgroup, for your helping hands and contributions to this project.

To my friends and neighbours, Ashley, Matt, and Dexter, thank you for welcoming me to Germany, and helping to make that transition easier. You are the reason I was able to visit home regularly, and I will be forever grateful.

To our colleagues and collaborators at GSI, thank you for your enthusiasm for collaboration, and for all of your help and support in the initial commissioning of the detection system. In particular, thank you to Joerg Lehnert, my primary point of contact, for enduring many emails and late nights of testing.

To Stephan Brons at HIT, thank you for your help in securing beam time, and for the support in adapting our setup to the clinical environment. Making measurements in a clinical facility was an incredible opportunity.

To Dennis Mücher, my advisor, the reason I am a researcher. Thank you for the opportunity to continue under your leadership when you came to Cologne. Thank you for helping to shape this project, and build the connections and network I relied on to complete it. Thank you for allowing the flexibility to visit family, and for always having my back in navigating the German bureaucracy.

To my parents, Julie and David Hymers, and my sister Meaghan, who have always believed in me. Thank you for your help as I moved across an ocean (twice!). Thank you for always being accessible when I needed to talk. And special thanks for the mountain of misplaced commas, typos, and mangled sentences that have been filtered out of all my important documents throughout the years.

Finally, to Matéa David-Steel, my partner and constant inspiration. Thank you for sharing with me the years of highs and lows, celebrations and sorrows, and enduring the long and frustrating writing process. I am so happy to have been able to share this chapter of my life with you, and I look forward to many more. Thank you for your constant and unyielding support, and for being my biggest cheerleader.

Contents

1 Introduction

Despite overall reductions in mortality associated with improvement in treatment options [1], cancer is the leading cause of death in most highly developed countries, and a top-three cause of death worldwide [2]. The burden of cancer is expected to rise significantly over the coming decades as communicable disease management improves, developing countries advance their standard of living, and global populations increase and age [1, 3]. While the most effective treatment varies with the type of cancer, approximately half of all cases will benefit from external beam radiotherapy (RT), either alone or in combination with other treatment modalities [4]. As the burden cancer places on the global healthcare system continues to increase, improvements in all areas of cancer management, including screening, prevention, treatment efficacy, and patient throughput, are of great importance. The aim of this thesis is to explore one possible improvement to the safety and efficacy of cancer treatment, without negatively impacting the number of patients which can be treated on a daily or annual basis.

1.1 Radiation Therapy

The guiding principle behind radiation therapy is the differential responses of cancerous tissue and healthy tissue to ionizing radiation. Several of the key 'hallmarks of cancer' are associated with genetic mutations originating in a single cell, and proliferating through the growth and division process of the nascent tumour [5]. Critically for RT, one potential cause of such mutations is exposure to ionizing radiation, leading to the possibility of secondary tumours being induced in the process of treating the first [6]. Therefore, the goals of an RT treatment plan are twofold: deliver a sufficient dose to the tumour to sterilize or kill all cancerous cells, thereby controlling the growth of the tumour; and spare as much normal, healthy tissue as possible from radiation exposure, in order to avoid complications caused by cellular damage or death [7].

Multiple mechanisms exist through which radiation can damage genetic material. The most straightforward is a direct ionization of the DNA (deoxyribonucleic acid) molecule, leading to structural deformation or a broken chemical bond which corrupts the genetic code. However, indirect ionization may also initiate these same pathways [8]. In this case, the ionization initiates on another molecule (such as water) forming a highly reactive

radical species. This radical may then interact with the DNA, removing an electron and transferring the ionization. The indirect nature of the interaction means that not every radical formed will necessarily lead to DNA damage [9]. However, since DNA comprises only a small fraction of the volume of each cell, indirect damage is believed to occur more frequently than direct DNA damage [10, 11].

Beyond the different ways in which DNA damage can occur, these effects may also be categorized as repairable or unrepairable damage. Given enough time, typically on the order of hours, repairable damage can be reversed, and the affected cells returned to a functional state. However, a rapid accumulation of several instances of repairable damage within the same cell may overwhelm the cellular self-repair mechanisms, leading to cell sterilization or death [12]. In contrast, a single instance of unrepairable damage is sufficient to cause the same effects [13]. The types of damage which are repairable, or the relative rates of repairable and unrepairable damage, are affected by a number of different factors, including the expression of DNA repair genes within the cell, the current stage of the cell within its mitotic life cycle, and the environment surrounding the cell [12, 14].

As tumour cells have undergone several mutations relative to a healthy cell, it is common that the DNA repair mechanisms in tumour cells are less robust than that of typical tissue [15]. Another factor making tumour cells more radiosensitive is the rapid cell division characteristic of malignancy: actively dividing cells are more susceptible to DNA damage, due to the replication of DNA during mitotic cell division [16]. This same factor also plays a role in determining which healthy cell types are most susceptible to radiation damage; for example, in tissues such as the gastrointestinal tract, where cells are rapidly replaced, radiosensitivity is increased similarly to tumours [17]. Environmental factors also play a role in determining the susceptibility of a cell to radiation; since indirect damage depends on the formation of radical species, environments favouring the formation of these radicals sensitize cells to radiation effects. As the most common radicals to form are reactive oxygen species, the presence of oxygen in the local cellular environment is a key factor in a cell's susceptibility to radiation damage. This effect is, unfortunately, typically associated with a reduction in tumour radiosensitivity. For large or fast-growing tumours, the rate of cell growth tends to exceed that of vascularization, leading to the central regions of the tumour being underoxygenated or hypoxic [18].

Differences in cell survival rate between tumours and other tissue types, after exposure to ionizing radiation, are modelled by the linear-quadratic (LQ) formula. This model uses the coefficient α to describe susceptibility to unrepairable damage, and β to describe susceptibility to repairable damage [19]. The logarithm of total cell survival S after exposure to a total radiation dose d is described by Equation (1.1). At low doses, the effect on cell survival is dominated by unrepairable damage α, but at higher doses, the

accumulation of multiple individually-repairable events β is the dominant contributor [20]. Different tissue types can be described by the ratio α/β, with more radiosensitive tissues such as tumours and some organs-at-risk typically having larger values of $\alpha/\beta \approx 10\,\mathrm{Gy}$, and healthy tissue of standard radiosensitivity having smaller values of $\alpha/\beta \approx 3\,\mathrm{Gy}$ [19, 21].

$$\ln(S) = -\alpha d - \beta d^2 \tag{1.1}$$

The LQ model and the inherent radiosensitivity differences between cell types inform the development of RT treatment plans. As the goal of treatment is to control the tumour by killing or sterilizing all malignant cells, while maintaining as much healthy tissue as possible, it is preferable to exploit the differences in response between cell types [20]. Therefore, it is uncommon to deliver the entire prescribed dose all at once, as such a treatment would be dominated by the β component, leading to the death of most irradiated cells, regardless of tissue type. While this method would certainly succeed in killing the tumour, it would not provide sufficient sparing of healthy tissue. Instead, treatments are often broken into fractions, with the total prescribed dose split over many irradiations delivered on different days. The prototypical example is a total prescribed dose of 70 Gy, split into 2 Gy fractions, delivered five days per week (typically Monday through Friday) for seven weeks [22]. Such a fractionation scheme allows sufficient time to recover from repairable β-type damage between irradiations, and spreads the total dose over a large enough time to allow initially-hypoxic regions in the interior of a tumour to be reoxygenated as the outer cells are sterilized or killed outright [23].

Recent studies in RT have discovered a phenomenon known as the FLASH effect, in which the damage to healthy tissue may be further reduced without affecting the rate of tumour control. When RT is delivered at ultra-high dose rates above $40\,\mathrm{Gy\,s^{-1}}$, the ability of healthy tissue to tolerate radiation is increased [24]. FLASH dose rates are several orders of magnitude higher than those employed in conventional RT, where a more typical dose rate is $2.0\,\mathrm{Gy\,min^{-1}}$ [25]. The enhanced radiation tolerance of healthy tissue to FLASH irradiation is projected to allow dose escalation to radioresistant tumours. Dose escalation has been shown to improve tumour control at conventional dose rates; however, dose escalation is must be implemented with extreme care using conventional RT, due to the increased danger of undesirable side effects caused by healthy tissue damage [26]. While the origin of the FLASH effect is not yet understood, and the underlying mechanism is debated, the potential impact is enormous. Clinical treatments do not yet routinely include the ultra-high dose rate irradiation needed to produce the FLASH effect; however, the phenomenon shows promise in improving both the safety and efficacy of treatment,

as well as facilitating higher patient throughput through shorter treatment times and a reduction in the total number of fractions (hypofractionation) [27].

1.1.1 Treatment Modalities

The most common method of delivering RT is the megavoltage X-ray source; however, the use of beams of charged particles, including protons and $^{12}C^{6+}$ ions, has also entered clinical practice [28]. Other heavy ions, such as $^{4}He^{2+}$, $^{16}O^{8+}$, and $^{20}Ne^{10+}$ (where 'heavy' refers to ions heavier than a proton), are also undergoing preclinical investigation, or have been used historically for treatment [29, 30]. A key advantage of these ion beams is their characteristic dose distribution, related to the variable stopping power of the ions as they lose energy quasi-continuously within the patient. The resulting dose distribution is inverted as compared to a photon beam, as shown in Figure 1.1, with a low entrance dose, rising to a sharp maximum at the beam endpoint, or Bragg peak (BP), followed by a very low (heavy ions) to nonexistent (protons) exit dose [30]. The exit dose with heavy ions is attributable to fragmentation of the primary beam, causing the nucleus to break apart into lighter fragments with a longer range [31]. This dose distribution offers clear advantages over the conventional photon RT, as the BP position may be easily adjusted by changing the beam energy. In this way, the BP can be placed directly on the tumour,

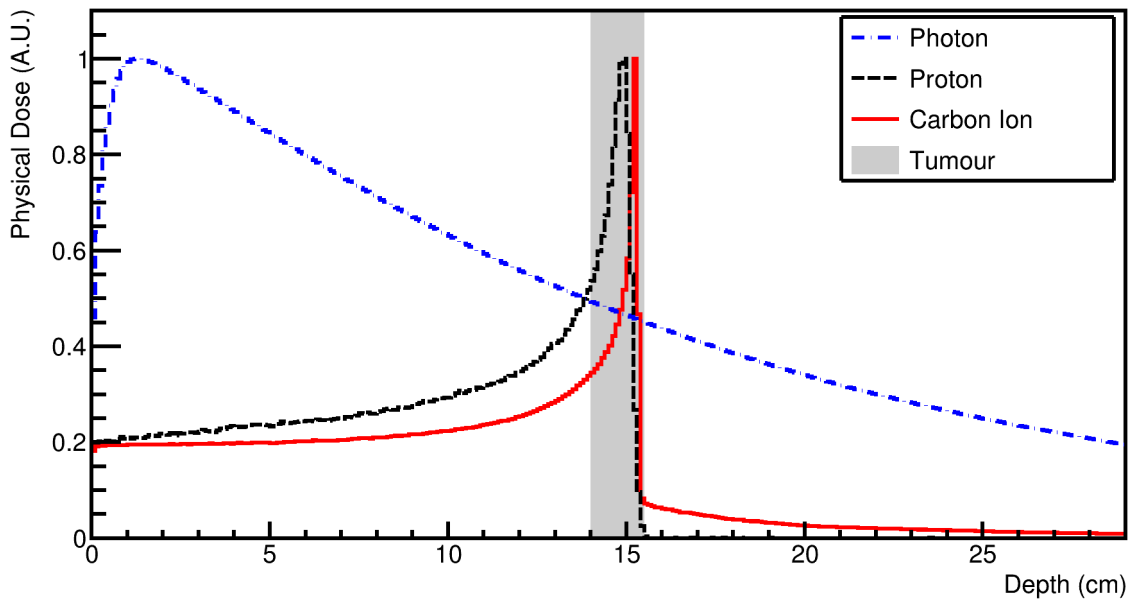

Figure 1.1: Normalized depth-dose distributions in water for several types of radiation used for external-beam therapy. The data for the 6 MV photons (blue) is experimental, while the proton (black) and $^{12}C^{6+}$ (red) distributions are simulated. Both ion species show the characteristic inverted dose distribution as compared to photons, allowing maximum dose to be applied to a tumour (grey). The Bragg peak is sharper for carbon ions, at the cost of a small exit dose due to fragmentation.

leading to a reduced dose to the surrounding healthy tissue [32]. This healthy tissue sparing is particularly important in protecting radiosensitive organs, such as the brain, spine, or bowel, which may be located near the beam path [33, 34, 35].

In addition to the advantages of the physical dose distribution, ion beams also offer radiobiological advantages over photon RT. The same variation in stopping power which produces the Bragg peak also directly affects the linear energy transfer (LET) of the treatment beam. Increases in stopping power and LET are tied to higher radiation damage, due to the more frequent energy transfer interactions and ionization events at higher LET [32]. This increase in the density of energy transfer increases the probability for a single particle to cause multiple instances of DNA damage within the same cell or nucleus, causing the same physical dose to have a higher relative biological effectiveness (RBE). However, at very high LET, the RBE becomes low again, due to an overkill effect [11]. Therefore, the dose distribution of heavy ions is doubly advantageous, both delivering the maximum physical dose at the BP, as well as increasing the biological impact of this dose maximum beyond what would be expected from the physical dose [36]. This elevated dose distribution negates some of the need for fractionated treatment, leading to an interest in hypofractionated ion beam RT, in which the same tumour control may be achieved with lower total dose, fewer irradiations, and a shorter overall duration of therapy [37].

In addition to the advantageous depth-dose distribution of ion beam RT, the lateral extent of an ion beam is well-defined compared to a photon beam. The charged nature of an ion beam allows electromagnetic focusing, which produces well-defined beamspots, compared to high-energy photons which are challenging to collimate and focus [38]. Although ion beams interact very frequently with the material through which they travel, the large forward momentum makes significant scattering relatively rare when compared to a photon beam, for which Compton scattering is the dominant interaction at the MeV energies typically employed in RT. Therefore, the dose distribution from an ion beam remains relatively well-defined, even for BP depths tens of centimeters inside a patient [30].

When comparing protons to heavy ions, the dosimetric advantages tend to increase with mass and charge. For instance, when comparing proton RT to carbon ion RT (CIRT), the carbon ion beam produces a sharper BP, exhibits a more pronounced increase in LET (and RBE) at the BP, and also maintains a sharper lateral dose gradient with less beam broadening due to the larger forward momentum of the heavier beam [30]. These properties of CIRT make it an appealing modality when the sparing of healthy tissue or radiosensitive organs at risk is particularly important [36]. For these reasons, CIRT is often used to treat tumours of the head and neck, where components of the central nervous

system such as the brain and spinal cord are the key organs at risk [39]. However, the benefits of CIRT apply to tumours located anywhere in the body [35]. The additional potential for sparing of healthy tissue also holds significant value in the treatment of pediatric patients, who are at the greatest lifetime risk for treatment-induced secondary tumours, due to their long potential post-treatment lifespan [40]. Heavy ions, such as carbon and oxygen, have also shown some enhancement in their ability to treat hypoxic or otherwise radioresistant tumours, due to the increased incidence of direct DNA damage at high LET [23].

1.1.2 Delivery of Carbon Ion Radiation Therapy

Producing the heavy-ion beams used in CIRT at sufficient energy to penetrate deep into the patient requires large and expensive particle accelerators, contributing to the additional cost of CIRT over photon or proton RT [41]. All current facilities performing clinical CIRT employ synchrotron-based accelerators to reach these high energies at clinically-relevant dose rates [42]. The primary component of a synchrotron accelerator is a continuous ring, through which particles may orbit. First, particles are injected into the synchrotron at a constant, low energy. This injection must be performed by another small particle accelerator, such as a linear accelerator, as a minimum energy is required to begin circulation within the synchrotron. During the filling process, the energy of the circulating beam remains constant [43]. Once the desired number of particles have been loaded into the ring, the acceleration process can begin. On each circuit, the particles pass through one or more radio frequency (RF) accelerator elements, increasing their energy with each revolution. As the particle energy increases, the field strength of the bending magnets which steer the beam through the ring must increase synchronously, to maintain a stable orbit within the accelerator. Furthermore, the frequency of the RF acceleration voltage must also increase synchronously with the increase in beam energy; the time taken to complete each revolution through the accelerator decreases as energy increases [44].

Once the beam has reached the desired energy, particles may be extracted. For conventional RT dose rates on the order of $1\,\mathrm{Gy\,min^{-1}}$, a slow extraction method is required, removing a fraction of particles from the accelerator at each revolution. By monitoring the intensity of the extracted beam, it is possible to adjust the extraction rate to maintain a stable average beam current for a period of several seconds [45]. However, due to the periodic nature of the circulating particles, and the sensitivity of the extraction method to small instabilities, the extracted beam typically has some microstructure, with variations up to 50 % in intensity being common [46]. After extraction is completed, any unused particles are dumped, emptying the accelerator prior to loading in the next set

of particles [47]. Due to the required pause in beam delivery to accelerate the next set of particles, synchrotrons are unable to provide a continuous beam. Instead, the beam is delivered in a pulsed structure, with each beam-on pulse referred to as a 'spill' [48]. The resultant beam structure is shown in Figure 1.2.

The beam produced by a synchrotron has a number of highly favourable properties for CIRT. Varying the beam energy between spills is simple, accomplished by merely selecting a different endpoint for the RF accelerator [44]. The beam intensity is stable and controllable, even within a spill, facilitating a wide variety of dose rates [45]. Finally, the extracted pencil beam is narrow and well-defined, allowing use of the lateral profile for sparing of organs at risk [30, 49]. However, typical tumours are larger both laterally and longitudinally than the single BP produced by this monoenergetic pencil beam. Therefore, clinical use of CIRT requires either expanding the single beam to cover the entire tumour, or delivering multiple beams to achieve the same full coverage [32].

The simplest approach to treating an entire tumour is to produce a broad, polyenergetic beam, which covers the full lateral and longitudinal extent of the target tumour, as shown in Figure 1.3a. Lateral beam broadening is achieved through scattering of the initial pencil beam in a multi-layered passive device, followed by collimation of the beam to maintain low divergence [50]. Additional patient-specific collimators are added to match the lateral

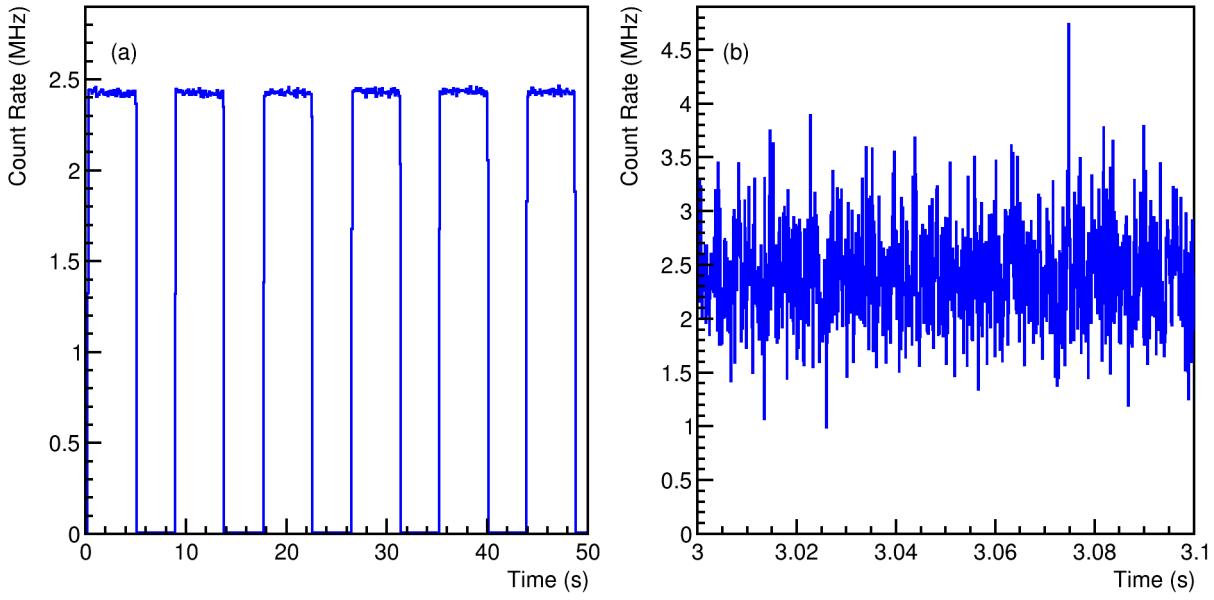

Figure 1.2: Synchrotron spill structure and microstructure. (a) Observed prompt count rates from a target irradiated by a clinical synchrotron accelerator used to deliver CIRT. Six spills were required to deliver the requested number of ions. The observed time structure is a consequence of the minimum time required to inject and accelerate a new batch of $^{12}C^{6+}$ particles. (b) Microstructure visible with a 100 µs bin size, showing the typical fluctuations in monitored beam intensity.

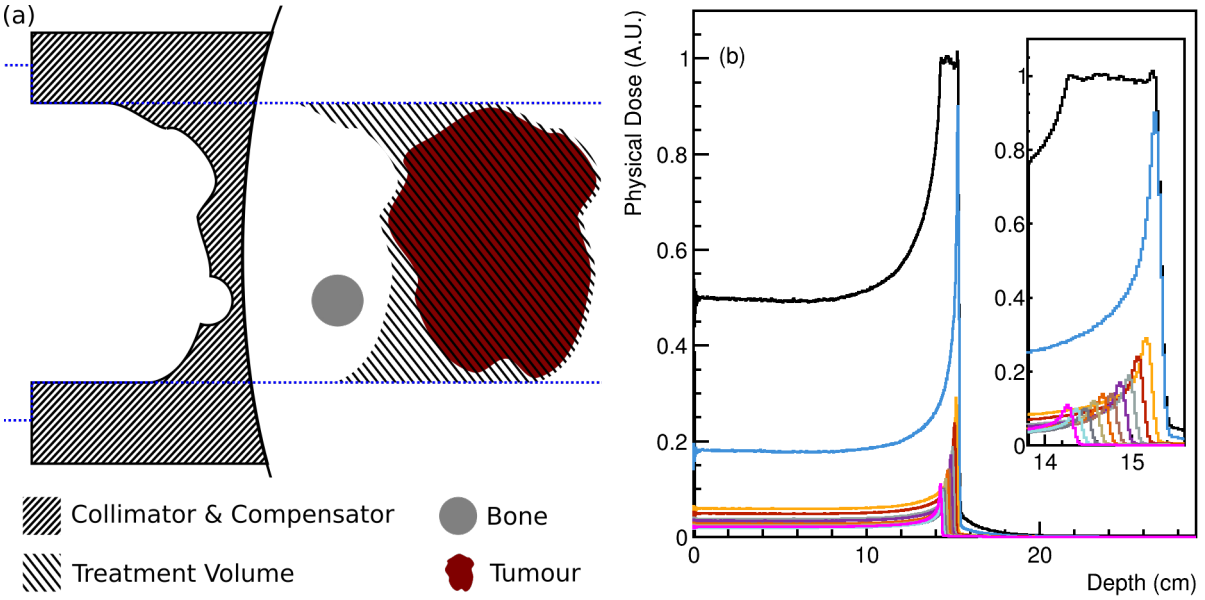

Figure 1.3: Dose distributions used in scattered CIRT. (a) Schematic of the dose distribution produced by a tumour-specific range compensator. The compensator is designed to conform the dose distribution from the polyenergetic beam to the distal edge of the tumour, taking into account the patient composition along the beam path. However, due to the constant width of the spread-out Bragg peak (SOBP), some healthy tissue superficial to the tumour is also irradiated, as the tumour is not a constant thickness over its entire volume. (b) Depth-dose distribution of a SOBP as compared to the pristine Bragg peak produced by the unmodified beam. The plateau dose of the SOBP is elevated as compared to the pristine Bragg peak, due to an accumulation of dose from multiple beam energies. The individual component Bragg peaks are shown in the inset.

beam profile to the contour of the tumour being treated. Longitudinal broadening may be achieved by modulating the energy of the primary beam, either by changing the target energy of the accelerator, or by inserting an attenuator to reduce the range of the beam in the patient [51]. Modern patient-specific collimators also include a specially-shaped attenuator matched to the profile of the tumour, such that the maximum depth at each position corresponds to the longitudinal profile of the tumour [52].

The effect of longitudinal broadening is the formation of a 'spread-out BP' (SOBP), which delivers multiple beam energies within the same spill, creating an overall dose distribution such as that shown in Figure 1.3b. One method of achieving this SOBP is with a variable-thickness wheel which intersects the beam, and spins rapidly during irradiation. As the wheel rotates, the thickness of the attenuator varies, rapidly modulating the beam energy to cover a fixed range of depths [51]. Another method of achieving a similar outcome is the ripple filter, a passive device with fine ridges or grooves inscribed on its surface. The varying thickness of the filter again leads to a polyenergetic distribution with a correlation between energy and position. However, the feature size of the filter is small

enough that the natural broadening of the beam as it travels through the patient results in a homogeneous dose distribution in the SOBP region [53].

The alternative to broad-beam irradiation is the use of several unmodified pencil beams at different energies and positions to achieve full longitudinal and lateral coverage of the target tumour. In this method, only monoenergetic beams are delivered, irradiating a layer of constant depth, as shown in Figure 1.4a, before switching energies to irradiate the next layer. As each layer is irradiated independently, it is straightforward to vary the lateral profile as a function of depth, facilitating a highly conformal dose distribution [7]. To achieve lateral coverage in each layer, the beam is actively scanned across the patient, as shown in Figure 1.4b, using powerful magnets to steer the pencil beam toward the specified location. This technique includes delivery of the beam to discrete, fixed locations (spot scanning), and continuous delivery of a moving beam (raster scanning). Both of these scanning methods provide the ability to vary the dose delivered as a function of position, as such a variation may be necessary to achieve a more uniform dose over the entire tumour [25].

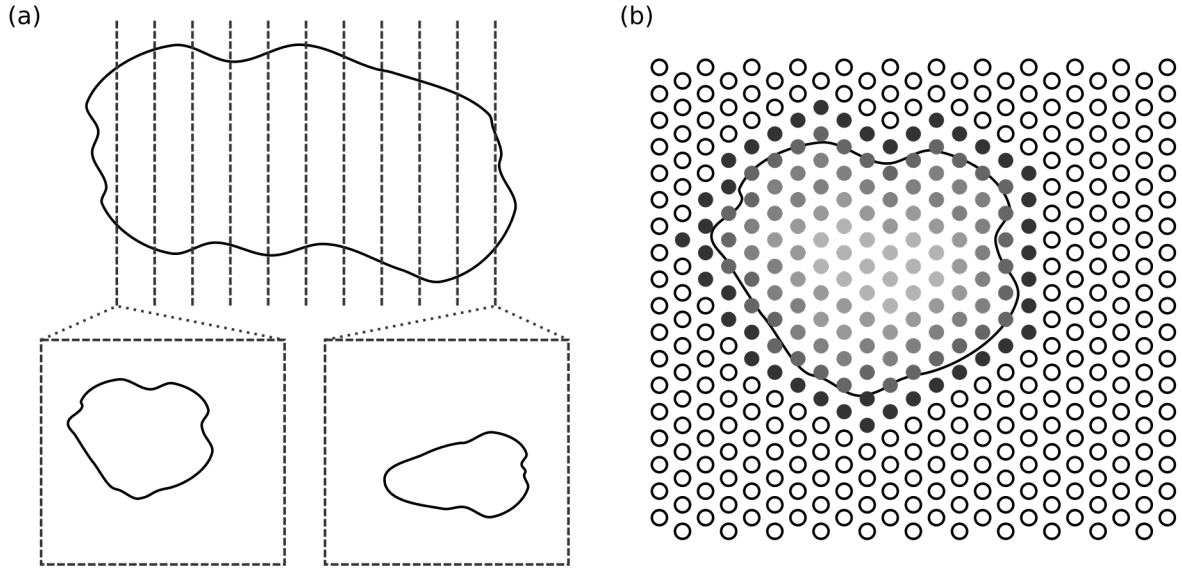

Figure 1.4: Schematic of scanned CIRT. (a) Longitudinal view of tumour, with slices marked. Each isoenergy slice may have a unique cross section. (b) An individual slice of the tumour, with spot scanning locations marked as either irradiated (solid) or unirradiated (hollow). Each spot may be irradiated with a different number of ions, as represented by the shading of the scan points, to produce a homogeneous dose distribution. In more superficial slices, some dose is also delivered from the plateau of deeper spots, as shown in Figure 1.3b, which must be taken into account during the treatment planning process.

1.2 Range Uncertainty

The improved conformity which can be achieved with CIRT comes with additional challenges which are not present in conventional photon therapy. The sharp BP requires precision in both the positioning of the beam and in selection of energy, which poses significant challenges. Beam range within a patient depends not only on the properties of the beam, but also on the path the beam takes through that patient. Variations in tissue composition, organ positioning, or the degree of filling in structures such as the lung, bowel, or sinuses affect the environment through which a treatment beam travels [54]. Variations such as respiration or other patient movement may occur during the delivery of a single fraction, while changes in patient positioning on the treatment table (on which they are positioned during irradiation) or variations in internal structures may occur between fractions delivered on different days [55]. These differences in composition can affect the stopping power of the treatment beam, leading to significant shifts in BP range, on the order of millimeters [56]. Patient-specific measurements are challenging, as typical imaging for treatment planning uses anatomical modalities such as x-ray computed tomography or magnetic resonance imaging, which do not experience the same interactions as an ion beam. Therefore, any estimation of ion stopping powers based on imaging is an indirect approximation, rather than a direct measurement, with further uncertainty involved in the extraction of stopping powers [57]. The consequences of failing to address this challenge are severe: errors in dose delivery mean that not only is the full tumour volume not treated, compromising tumour control, but an increased amount of healthy tissue is also irradiated. This increased dose to healthy tissue corresponds to an increased incidence of side effects, including the later development of secondary, treatment-induced, tumours [6].

To account for these uncertainties in dose delivery, a safety margin is added around the tumour volume during the planning process, to account for an error in BP position up to a few millimeters in any direction; for example, a typical safety margin in the adult head is 3.0 mm [56]. While such a safety margin does ensure that the entire tumour is irradiated with the full prescribed dose, it also results in a significant volume of healthy tissue being guaranteed to experience this full dose as well. These safety margins, and the inherent uncertainty in BP positioning, also limit the ability of oncologists to develop treatment plans which take full advantage of the rapid longitudinal falloff in dose beyond the Bragg peak. Instead, where radiosensitive organs are located close to tumours, the direction of irradiation is selected such that range errors on the order of millimeters maintain acceptable sparing of organs at risk. These additional constraints can complicate the treatment planning process, leading to difficulty in optimizing a dose delivery plan [33].

1.3 Range Monitoring

To address the challenge of range uncertainty, the field of range monitoring (RM) has formed, with the goal of developing methods of measuring BP position or dose distribution during or immediately after irradiation. The data accumulated from RM has many uses, including the refinement of models for predicting BP position, and verifying that a given treatment has been delivered successfully [36]. In the ideal case, RM could deliver immediate feedback on BP depth during irradiation, allowing a treatment to be aborted if a range error is detected [58]. As the safety margins in CIRT treatment plans are already on the order of millimeters, the ideal RM method would also provide sub-millimeter accuracy, to allow meaningful shrinkage of these margins and a reduction in the dose to healthy tissue, while maintaining the current rate of tumour control [59, 60, 61]. Particularly for scanned treatments, this ideal method would also allow monitoring of each individual BP position [62].

RM methods are classified into two broad categories. Absolute RM provides a direct measurement of a BP position or dose distribution, which may be correlated to anatomical imaging, such as that acquired during treatment planning. This direct correlation to patient anatomy means that absolute RM is sufficient to determine whether a treatment has properly covered the tumour region [63]. However, achieving a high level of accuracy in absolute RM is particularly challenging, due to additional sources of uncertainty relating to the alignment of two separate images [64]. Relative RM measures only differences in BP position between two beams or irradiations, without a direct correlation to the absolute position of the tumour. These comparisons may be made between between two different fractions (i.e. inter-fraction), or two different beamspots within the same fraction (i.e. intra-fraction). The strength of relative RM is its ability to measure deviations in patient positioning or internal structure, which often occur between irradiations (inter-fraction), and may also occur during dose delivery (intra-fraction) [65].

A number of RM implementations have been proposed, many of which rely on secondary radiation produced by beam-patient interactions. Although several of these approaches have been studied in detail, including through clinical trials, no method has yet been integrated into widespread clinical practice.

1.3.1 Positron Emission Tomography

The most mature RM techniques use positron emission tomography (PET). However, unlike conventional PET, in which a positron emitter is injected into the patient, PET

RM depends on the activation of patient tissue or beam-like fragments to form positron emitters [65]. The PET signal from these activated regions then provides insight into BP positioning. As several positron emitters commonly produced in CIRT, including ^{11}C and ^{13}N, have lifetimes on the order of tens of minutes [66], the simplest implementations of PET RM involve moving patients to a conventional PET scanner after irradiation. However, delaying data collection by moving the patient to another room, or even to a different position within the same room, places limits on collectable statistics, and decreases accuracy due to biological processes moving positron emitters away from the site of formation – so-called 'washout'. Furthermore, when data collection begins only after an entire fraction is delivered, only an integrated measurement of the total dose distribution is possible; there is no way to independently assess each BP position [64]. More modern approaches, known as 'in-beam PET', have integrated PET systems into the treatment table. This integration allows data collection to occur during the most active timeframe, collecting either more total data or the same amount of data in less time, along with significantly improving sensitivity to shorter-lived positron emitters such as ^{15}O [66]. In-beam PET can also provide some intra-fraction monitoring, due to data collection taking place during irradiation, or during spill pauses of a synchrotron accelerator [67]. Several clinical trials of PET RM for CIRT have been conducted. One current trial, at the Italian National Center of Oncological Hadrontherapy (CNAO, Pavia, Italy), studies in-beam PET as part of the INSIDE project. While this trial is still ongoing, results from the first phase have demonstrated a sensitivity to BP range differences of 3.7 mm when applying relative RM to CIRT for tumours of the head and neck [68].

1.3.2 Prompt Gamma

An alternative to PET, based on similar principles, is prompt gamma (PG) imaging. While both PET and PG monitor gamma ray photons, PG is capable of using all photons, including those emitted by prompt reactions, rather than being limited to the correlated and delayed 511 keV annihilation photons produced by positron emission. Therefore, the available signal for PG RM is stronger than in PET [65]. PG may also in principle operate with less bulky detectors than PET, as coincidence detection with 180° separation is no longer required. However, the lack of this coincidence detection means that some other mechanism is required to constrain the origin of the detected photon, as this constraint is necessary to correlate the PG signal to BP position.

One method of extracting trajectory information in PG imaging involves adding a physical collimator to the detector. This approach constrains the origin of the photon to a narrow slice of the patient directly in front of the detection system, by absorbing

photons which approach from other directions. However, the thick collimators required to attenuate high-energy photons with energies on the order of MeV significantly reduce the detection efficiency of PG systems, due to the limited field of view [69]. An alternative to physical collimation is electronic collimation, using coincident detection of multiple photon interactions in a Compton camera. This method requires the same photon to interact twice, scattering in a first detector layer, and interacting further in a second detector layer. Using the known dynamics of Compton scattering, it is then possible to constrain the incoming trajectory of the photon to a conical shell [65]. These estimates can be further refined using knowledge of the approximate path of the treatment beam, as well as the agreement of multiple detection events [70]. Although the use of electronic collimation does bypass the efficiency challenge of a physical collimator, a new efficiency challenge is the need for coincident detection of multiple interactions of the same photon.

Physical and electronic collimation have both been successfully applied to PG RM for proton radiotherapy. However, applying the same methods to CIRT poses significant challenges. While the total gamma ray production cross sections are similar for proton and carbon ion beams, the physical dose and RBE of the $^{12}C^{6+}$ is significantly higher than the proton, as discussed in Section 1.1.1. Therefore, an order of magnitude improvement in detection efficiency would be required to reach the same precision for PG RM in CIRT as has been demonstrated for proton radiotherapy [71]. Achieving such an improvement in efficiency and count rate capability would require revolutionary breakthroughs in photon detectors.

1.3.3 Interaction Vertex Imaging

Another RM method which uses only prompt secondary radiation is interaction vertex imaging (IVI), which is the focus of this thesis. Unlike the previously-discussed RM methods, which both monitor photons, IVI exclusively uses charged particles, typically protons [72]. As with other RM modalities, the secondary charged particles of interest are produced by beam-patient interactions; for IVI, these are typically fragmentation reactions which break the primary beam into several lighter particles. IVI is only viable for heavy-ion RT, such as CIRT, due to the requirement that the fragment have a longer range than the primary beam, in order to escape the patient. This constraint dictates that the fragments must have a lower stopping power than the primary beam, and receive a significant fraction of the beam energy, neither of which is possible in proton radiotherapy.

Although a significant fraction of secondary protons are unable to exit the patient due to their quasi-continuous energy loss along the exit path, the detection efficiency of charged

particles once outside the patient is much greater than that of photons, approaching 100 %. The high detection efficiency of charged particles also facilitates multiple coincident detection events for the same particle, as with the Compton camera. As charged particles are expected to follow a ballistic trajectory, two sensor layers in a tracker configuration is sufficient to constrain the trajectory to a line, as with the coincident detection of annihilation photons in PET RM. This trajectory information, along with knowledge of the direction of the treatment beam, is used to reconstruct the location of the reaction which produced the tracked fragment [62]. The resultant reconstructed site is termed the 'interaction vertex', leading to the name IVI. Although the tracking and reconstruction processes are simplified for IVI as compared to other RM methods, the resolution of IVI suffers due to multiple Coulomb scattering of the fragment as it exits the patient. This effect limits the precision with which a single interaction vertex can be reconstructed [73]. The continual interaction of these charged fragments as they exit the patient also leads to another key limitation of IVI: as the fragment must exit the patient with sufficient energy to reach external detectors, IVI is not sensitive to interactions occurring at or near the BP, with the limit of sensitivity depending on the amount of material the fragments must traverse before reaching the detection system [62].

A number of investigations have previously studied IVI methods for range monitoring in CIRT, with a focus on relative RM [60, 74, 75]. High precision has been achieved by implementing a software filter into the interaction vertex reconstruction process, which preferentially rejects interaction vertices for which the inaccuracy introduced by multiple Coulomb scattering is most significant. This approach is named 'filtered IVI' (fIVI) after the software filter aspect [76].

Two implementations of IVI are currently undergoing clinical trials. A tracker composed of a large, multilayer scintillator volume, known as the 'Dose Profiler', was developed at CNAO. It is currently being tested as part of the INSIDE project, along with the in-beam PET system discussed in Section 1.3.1 [54]. Another device, developed and tested at the Heidelberg Ion-Beam Therapy Center (HIT, Heidelberg, Germany), consists of an array of seven small two-layer trackers composed of thin silicon detectors, each with a sensitive area of $2.8 \times 1.4\,\mathrm{cm}^2$ [56]. Both of these trials investigate relative RM in the context of tumours of the head and neck.

Another promising IVI implementation, which combines the strengths of both devices currently in clinical trials, has been previously proposed by the author [76]. This proposed device is a single large tracker, which combines the large sensitive area of the multilayer device tested at CNAO, with the speed and precision of thin silicon sensors, like those of the system tested at HIT. Achieving a large and highly rate-capable sensitive area with a single tracker allows greater flexibility in positioning the device around a patient,

to account for variations in size or tumour position, as opposed to an array of smaller trackers, which is more restrictive due to the common focal point. The large sensitive area also maximizes the data collected, which is important to perform RM subject to the dose constraint of clinical irradiation. This device also has the potential to support operation at sufficient interaction rates to extend IVI RM to ultra-high dose rate FLASH RT.

This thesis describes the hardware selection, design, and initial testing of the prototype fIVI Range Monitoring System, including the measurement of clinical beams in plastic phantoms representative of the human head and torso. To analyze the collected data, an updated, parallel implementation of the fIVI reconstruction algorithm is detailed. This system is capable of achieving millimetric precision in the determination of BP depth differences under clinical conditions, within 200 ms after delivery of a single beam spot. This high precision is maintained for the challenging case of shallow BP positions, in which fewer secondary protons are produced. These results strongly support the suitability of fIVI for online monitoring of CIRT treatments, as well as a possible safety interlock which would allow a reduction in the margin of irradiated healthy tissue around a tumour.

2 Commissioning of the Detection System

2.1 Silicon Detectors

Silicon diode detectors are a common choice for applications involving the tracking of charged particles [74, 77, 78]. These thin sensors, available in thicknesses on the order of 100 µm, are unlikely to cause significant deflection in tracked particles, which could affect the performance of fIVI reconstruction. Silicon detectors are commercially available in a variety of sizes; for the largest such sensors, only a small number would be required to reach total sensitive areas on the order of $100\,\mathrm{cm}^2$, matching the requirements identified for RM applications [76]. Silicon sensors are also capable of achieving high data rates, with the inherent signal rise time in response to a charged particle being on the order of ns [79].

2.1.1 pn Junction

The basic operating principle of the silicon diode detector is based on the formation of a semiconductor pn junction. Unlike a conventional conductor, in which conduction electrons are freely mobile within the lattice structure of the material, a semiconductor resembles an insulator, in that electrons require some excitation in order to separate them from their lattice sites and allow motion. However, the required excitation energy in a semiconductor is sufficiently low that this excitation can occur thermally, at or below room temperature. When electrons are excited into the higher-energy conduction band from their ground state valence band lattice sites, a space, known as a 'hole', is left in the valence band. Other bound electrons may then transfer into these holes from adjacent lattice sites, without requiring excitation out of the valence band. This hole can be modelled as a carrier of positive charge, in the same way that an electron is a carrier of negative charge. Therefore, the flow of current in a pure semiconductor such as silicon has significant contributions from both electrons and holes, as the number of conduction electrons and holes will be equal [80, 81].

The addition of trace amounts of other elements, or the formation of defects in the crystal lattice of the semiconductor, can cause changes in the balance between electrons and holes. When these elements are purposefully added to alter the properties of a semiconductor, they are referred to as 'dopants', and the process of their addition is called 'doping'. Two types of doping may occur, to increase the contributions of electrons or holes. Substituting a single silicon atom for a different element with an extra valence electron, as shown in Figure 2.1a, will result in an extra, unpaired electron which does not take part in the formation of lattice bonds. This extra electron can therefore be more easily excited to form a conduction electron and, importantly, does not leave behind a hole in the structure of the crystal lattice. The result of adding such dopants is a shift in the balance of conduction, towards electrons and away from holes. The resulting semiconductor is known as 'n-type', as the dominant current-carrying species is the negatively-charged electron. Similarly, substitution of a silicon atom for a different element with one fewer valence electron, as shown in Figure 2.1b, will produce a hole without the corresponding conduction electron. In this case, the positively-charged hole will be the dominant current-carrying species, and the resultant material is called 'p-type' [80, 81].

When an n-type material and a p-type material are placed into physical and electrical contact, known as a 'pn junction', there is a tendency for conduction electrons to migrate from the n-type material into the p-type material, filling the holes. This process creates

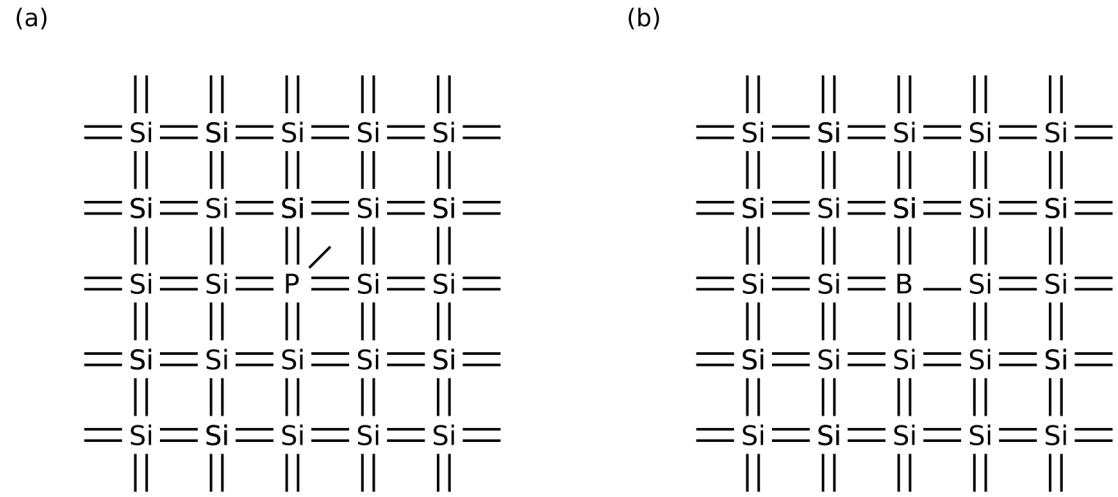

Figure 2.1: Crystal lattice structure of n and p type semiconductors. (a) n-type silicon, with donor-type dopant (phosphorus), including an additional electron not involved in lattice bonding, which is easily excited to become a conduction electron. Electrons are the primary charge carrier. (b) p-type silicon, with acceptor-type dopant (boron), causing a hole to appear in the electron structure, with no corresponding excited conduction electron. Holes are the primary charge carrier.

a region free of charge carriers, known as the depletion region, in which an electric field is formed due to the charge distribution formed by the recombination of electrons and holes around dopant atoms [81]. This electric field opposes further movement of charge carriers across the junction, effectively producing a high resistance to current flow in a single direction. Any spontaneous formation of electrons or holes within the depletion region are rapidly separated by this field, drawing electrons toward the n-type region and holes toward the p-type region, generating a small current [82].

If an appropriate external potential is applied across the pn junction, supporting the natural electric field, the size of the depletion region may be increased. In a silicon detector, it is typical to apply sufficient voltage that the depletion region extends through the entire thickness of the detector [83]. When a charged particle passes through the sensor, it deposits energy in the semiconductor lattice, exciting electrons and creating mobile charge carriers within the depletion region. The potential at the pn junction, plotted in Figure 2.2, rapidly separates these charge carriers, and the resultant charge or current is recorded as an interaction in the detector. This process gives rise to the inherent nanosecond timing performance of silicon detectors, as the signal formed by this charge separation has a fast rise time [79].

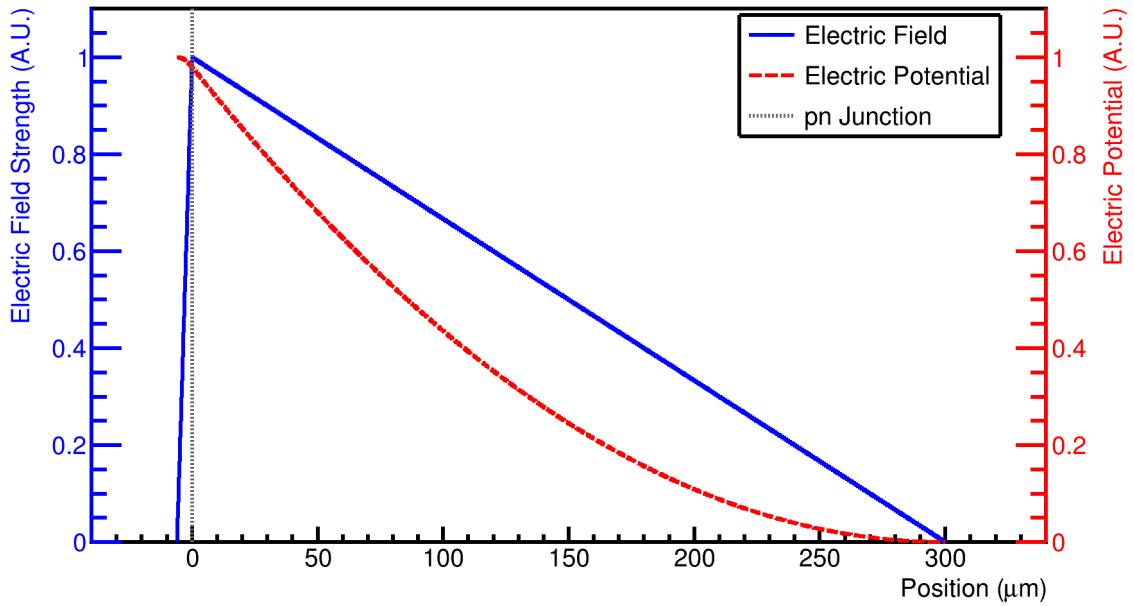

Figure 2.2: Electrical properties of a pn junction. The plotted field represents a thin, but heavily-doped, n-type region on the left, in contact with a thick, but lightly-doped, p-type region on the right. The field is strongest at the contact point between the regions. As an equal number of charge carriers cross the junction in both directions, the field extends further into the lightly-doped region than the heavily-doped region.

A typical silicon diode detector is formed from a silicon wafer which is lightly doped throughout its entire volume. A thin layer on one surface of the wafer is then heavily doped with the opposite polarity, forming the pn junction [84]. Electrical contacts are then made on both surfaces, to allow the application of the external reverse bias voltage, and the measurement of charge or current pulses formed in response to particle interactions. Therefore, when discussing these sensors, it is common to refer to the p side and the n side, reflecting the doping of that side of the sensor. The exact form of the electrical contacts on each side of the sensor varies depending on the application for which a detector is intended [85, 86, 87].

2.1.2 Detector Characteristics

Several mechanisms exist to achieve position sensitivity in thin silicon detectors, as is required for tracking applications. One option is physical segmentation, in which the sensitive area of the detector is broken down into smaller independent regions. One common segmentation scheme is strip segmentation of one or both sides of the sensor, using long and narrow electrodes that will collect charge carriers primarily from interactions which occur directly beneath the sensitive region [85]. If both the p and n sides of the same sensor are segmented along different axes, it is possible to determine the position of an interaction based on the combination of segments which are excited [84]. Another common approach is the pixel detector, in which the entire sensitive area of the sensor is broken into discrete elements, which may operate completely independently [87]. A third approach does not require physical segmentation at all, but instead relies on the lateral drift of charge carriers, orthogonal to the pn junction and the bias potential, to reconstruct the position of an interaction. As this approach provides position sensitivity within an individual detector element, sensors using this model are referred to as 'position-sensitive detectors' (PSDs) [88].

Position sensitivity in the PSD is accomplished through a measurement of the partitioning of charge between electrodes positioned on opposite edges of the same surface of the sensor, as shown in Figure 2.3a. The position of the interaction is proportional to the degree of charge sharing [86]. While the required number of readout channels for such a sensor is fixed, regardless of the sensor size, the lack of segmentation poses a challenge regarding rate performance. As the entire sensitive area of the sensor is combined in a single readout system, it is impossible to reconstruct two coincident interactions anywhere within the sensor, as the signals from the two interactions will be combined during readout [89]. Therefore, these devices become rate-limited at much lower count rates than physically-segmented sensors. There is also a position-dependent variation on the order of 100 ns

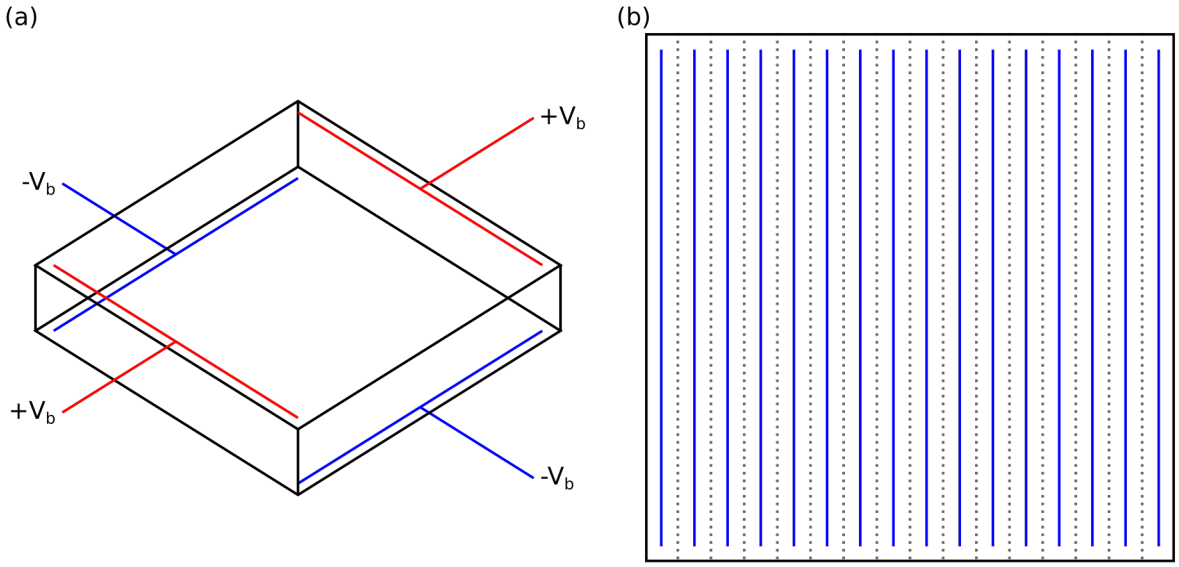

Figure 2.3: Schematic of readout and biasing schemes for silicon sensors. (a) Position-sensitive detector. Electrode positions are indicated on both the p side (blue) and n side (red) of the sensor. A symmetric bias $\pm V_b$ is applied across the sensor, using the same electrodes as for readout. The total bias voltage of $2V_b$ forms the depletion region between the two lateral faces. Asymmetric biasing is also possible, through applying a total bias voltage V_b to one face only, and holding the other face at ground. Rapid separation of charge occurs across the thickness of the sensor, but once charges have reached either surface, they must diffuse laterally within a resistive layer to be collected by the electrodes. As each side of the sensor is position-sensitive along a different axis, two-dimensional position resolution sensitivity is possible. (b) Schematic of the p side segmentation of a strip-segmented detector. Electrode positions (blue) and the approximate boundaries between segments (grey, dotted) are indicated. As in (a), the bias is applied through the readout electrodes. As each electrode spans the full length of each segment, the influence of the lateral drift of charge carriers is significantly reduced as compared to a position-sensitive detector.

in the time difference between signals at different electrodes, due to the resistivity of the sensor. This variation necessitates the use of long coincidence windows to correctly reconstruct interactions across the entire sensor. Therefore, an upper bound exists on the count rate which can be measured with a position-sensitive device, which is significantly lower than the rate capability of a segmented sensor [90]. In order to allow measurement at any conventional dose rate, along with the potential to extend IVI RM to FLASH dose rates, only devices with physical segmentation were considered for the prototype fIVI Range Monitoring System.

Physically-segmented sensor designs are also capable of providing excellent spatial resolution, due to the possibility of producing small segments with dimensions on the order of 10 µm [87]. These sensors also allow higher rate capabilities than PSDs, as each segment may be read out individually, reducing the cases where multiple interactions

are confused with each other. Here, pixel detectors offer a distinct advantage over strip-segmented detectors, as the sensitive area of each pixel is smaller than a strip which spans the full length of a sensor, as shown in Figure 2.3b. Strip-segmented detectors also exhibit the further disadvantage of requiring a coincidence between either the two sides of a double-sided sensor, or between two single-sided sensors, in order to reconstruct the position of an interaction; for pixel sensors, no coincidence is required [84].

However, the enhanced rate performance of a pixel sensor comes at the cost of a higher number of electronic channels required to read out the same sensor. With a strip-segmented sensor, the total number of channels scales with the perimeter of the sensor, while with a pixel sensor, it scales with the total sensitive area. For large sensitive areas, the total number of channels required for a pixel setup grows rapidly, placing higher requirements on the processing capacity needed to manage these channels [91]. As one of the goals of the proposed setup is to achieve online RM, increasing the number of channels is unfavourable, as this increase would be expected to require more online processing, with more detrimental scaling to large sensitive areas. Therefore, strip-segmented silicon detectors offer a reasonable compromise between rate capability and maintaining a manageable total number of electronic channels. As there is not expected to be a large difference in performance between single-sided and double-sided segmented sensors, double-sided segmentation is preferred due to requiring a smaller total number of physical sensors, facilitating an overall smaller detection system.

Due to limited space in the treatment room, a smaller detection system is highly favourable for integration with clinical practice [61]. Similarly, consideration must be given to the readout system for the double-sided strip-segmented sensors. Conventional readout systems are typically limited in the number of channels which can be processed in a single module, requiring a significant amount of bulky signal processing hardware to be located close to the detector [91]. Such a solution would be difficult to incorporate into a clinical workflow, as the space close to the treatment table is often restricted by the need to move patients in and out of the treatment area, or must be dedicated to other hardware involved in treatment, such as respiratory gating [92]. Therefore, only detection systems using integrated digital readouts were considered. Fully digital systems can be highly miniaturized and integrated closely with the sensor, allowing readout of a large number of channels without requiring excessive space for data processing hardware [91].

One additional consideration is required for the readout system. Beyond the inherent response time of the silicon diode, it is necessary to select a readout system which minimizes the time required to integrate and digitize the raw signal. This optimization is particularly important when considering strip-segmented sensors, as the sensitive area of a segment is large compared to a pixel. Therefore, achieving a short dead time, during

which no other events can be processed in the same segment, is expected to have a significant impact on the achievable count rate. However, short processing times are inherently related to poor energy resolution, as a shorter processing time means that there is less ability to average out the effects of noise, which arises from processes such as the spontaneous thermal excitation of charge carriers within the depletion zone [81]. If the energy resolution were important for fIVI, this impact on precision would pose a significant problem. However, previous studies have achieved good performance without including any energy information at all, indicating that the effect of reduced energy resolution is not expected to be detrimental to the system's overall performance [76].

2.1.3 Selected System

The sensors developed for the Silicon Tracking System (STS) of the Compressed Baryonic Matter (CBM) experiment, which will be installed at the Facility for Antiproton and Ion Research (FAIR, Darmstadt, Germany), exhibit excellent agreement with the requirements of the fIVI Range Monitoring System. The STS uses double-sided strip-segmented silicon sensors, with a width of 6 cm, and sensitive areas ranging between 12 cm^2 and 72 cm^2, along with a fully-digital, high-rate readout system [93]. These sensors are finely segmented, with a 58 µm center-to-center pitch, providing excellent spatial resolution, and dividing the large sensor area into 1024 independent segments per side. Due to the use of axial strips on the n side, and angled strips on the p side, all connections to readout electronics may be made on a single 6 cm edge [94]. The readout system provides a timestamp resolution on the order of ns, and is designed to handle event rates up to 250 kHz per segment when installed at the CBM [95]. For the prototype fIVI Range Monitoring System, a subset of this full rate capability has been implemented, which is expected to meet the demands of clinical RM.

2.2 Physical Design

2.2.1 Sensor Module

Several changes were necessary to adapt the mounting system of the CBM sensors for the prototype fIVI Range Monitoring System. These sensors were designed to be mounted in large ladders, with several sensors stacked to produce an overall height of up to 50 cm [96]. This design constraint of the STS necessitated the use of long analog cables connecting the sensor to the front-end electronics, tens of centimeters away. While this constraint

did not prevent the use of these sensors for fIVI, it did require the support frame for the sensor and front-end electronics to be larger than otherwise necessary.

The module frame into which components were mounted was required to hold the front-end electronics at a fixed position relative to the sensor. This requirement was necessary to maintain the parallel and shielded nature of the analog microcable bundles connecting the sensor and front-end electronics. The frame design used in the prototype fIVI Range Monitoring System is based on a temporary carrier frame used during the CBM commissioning process, prior to final installation of each sensor. However, the sensor mounting had to be adapted to a permanent use case, which was achieved by replacing the mounting structures which obstructed the sensitive region of the sensor.

The basic shape of the sensor module is a rectangular aluminum frame, with the microcables oriented along the long axis of the rectangle. At one end, the sensor is installed, mounted to a poly-ethyl ether ketone (PEEK) backplate. A different backplate design is required for each size of sensor to provide maximum support, and to align the center points of different sensor sizes in the same position relative to the module frame. The backplates are precisely machined to match the dimensions of the sensitive area of each sensor; they overlap only the insensitive guard ring region at the edge of the silicon wafer. During the mounting process, the sensor is placed on the backplate, supported only at its edge, and adhered with epoxy resin in each corner. The backplate is then attached to the frame, using 35 mm standoffs.

The other element which must be installed in the module frame is the bracket which supports the front-end electronics. Two key constraints exist on this design. The first is that these electronics may dissipate up to 50 W per module, and are quite temperature-sensitive. Therefore, provisions must be made to remove this heat and maintain a low temperature, to allow sustained sensor operation. The second is that the positioning of the front-end electronics relative to the sensor must be chosen to accommodate the analog microcables which connect the two components. These cables are highly sensitive to noise, and are therefore bundled together and shielded [97]. To maximize the efficacy of this shielding, the cables must run in a straight line, without being allowed to buckle. Therefore, the exact positioning of the front-end electronics will be different for each combination of sensor and microcable, and is sensitive to even small variations in the positioning of the installed sensor. To accommodate both of these requirements, the front-end electronics are mounted to an aluminum backplate, installed onto the module frame, which supports the installation of a cold plate for liquid cooling. The position of this backplate may be adjusted along the long axis of the module frame using slotted mounting holes, to allow fine-tuning of the separation between the sensor backing and front-end electronics to exactly match the cable length.

Two additional features have also been added to the module, to improve safety and stability. Two Delrin clamps are installed along the path of the analog microcables, to hold the cable bundle together and to further reduce the potential for buckling or separation. A front frame is also attached, separated from the rear frame by 50 mm standoffs. Including both frames, but excluding the portion of the liquid cooling mounting plate which extends beyond the frame, the total thickness of the module is 60 mm. Although the front frame does not provide a mounting position for any integral components of the module, it allows the module to be freestanding in multiple orientations, and provides some protection against incidental contact with the sensitive microcables during module installation. A completed module is pictured in Figure 2.4.

2.2.2 Enclosure

To fix the two sensor modules into a tracker configuration, brackets are installed between the two layers of the frame, using the threaded holes near the corner of each module. These brackets provide a flat mounting surface which may be installed parallel to any of the four lateral edges of the sensor. Two baseplates have been manufactured, one for upright mounting of the modules, secured along the short edge closest to the front-end electronics, and one for lateral mounting of the sensors, secured along the long edge of the modules. The lateral configuration also allows for offset mounting of the two sensors, such that the sensors may be aligned at their center points, or at either of the 6 cm edges. In contrast, the upright configuration forces the sensors to be aligned at their center point, due to the design of the module frame. In all configurations, the two modules are mounted parallel to each other and to the edges of the mounting plate, 12.0 cm apart. Although both configurations have been manufactured, all testing to date has been conducted solely in the upright configuration.

To protect and enclose the two sensor modules, a cage has been developed to surround the two modules. This cage consists of an aluminum support frame, as shown in Figure **??**, along with 1.0 mm thick aluminum panels. The support frame may be mounted to either the upright or lateral baseplate, with a different set of covering panels installed, based on which sides remain exposed. The dimensions of this enclosure, excluding the baseplate, are 257 mm × 257 mm × 436 mm. The purpose of the covering panels, shown installed in Figure **??**, is to protect the sensors from exposure to visible light, which may produce noise in the silicon detectors, as well as providing a shield to block low-energy particles, such as electrons produced by the ionization of air. These secondary electrons follow chaotic paths, scattering frequently, and do not carry useful information related to the BP position. A black anodized coating reduces the reflectivity of optical photons

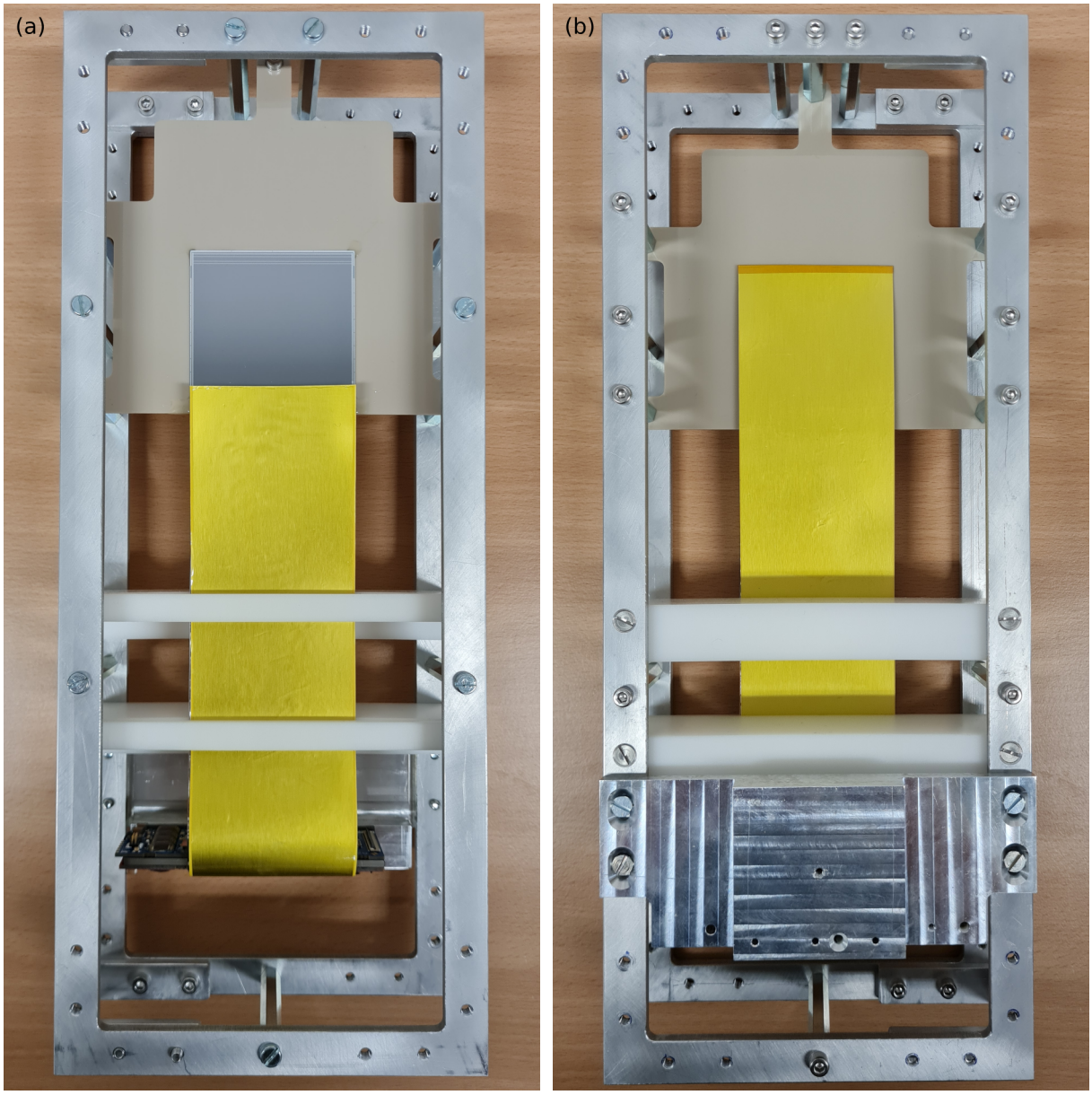

Figure 2.4: Photograph of assembled sensor module. The $6 \times 6\,\mathrm{cm}^2$ sensor module is pictured from (a) the front, and (b) the rear. The exterior dimensions of each frame are $374\,\mathrm{mm} \times 150\,\mathrm{mm}$. The square feature on the lower rear is the mounting location for a cold plate, which is used to moderate the temperature of the front-end electronics, visible on the lower front.

as compared to uncoated aluminum, reducing the likelihood of reflected photons passing through interfaces between panels and reaching the interior sensors. The entire cage is electrically connected, through the conductive fasteners and removal of the anodization layer at the fastener locations. This electrical continuity produces a Faraday cage, which is intended to reduce the susceptibility of the analog signaling to electromagnetic interference when the enclosure is grounded. However, the required gaps in this cage make such isolation imperfect.

One of the covering panels contains two cutouts in which 5 mm thick passthrough panels are installed, with each panel containing the necessary connections for power, control, readout, and cooling of a single module, as shown in Figure 2.5. These panels are thicker than the other side walls to provide sufficient material to mount the electronic and hydraulic feedthroughs. Several covering panels have been manufactured, to account for the different relative positions of the sensors in the various lateral and upright configurations. Designing the passthrough panels and associated cover plate as two separate pieces allows the electrical and cooling connections to remain attached to the module, and to be repositioned for different sensor configurations. To limit the size of

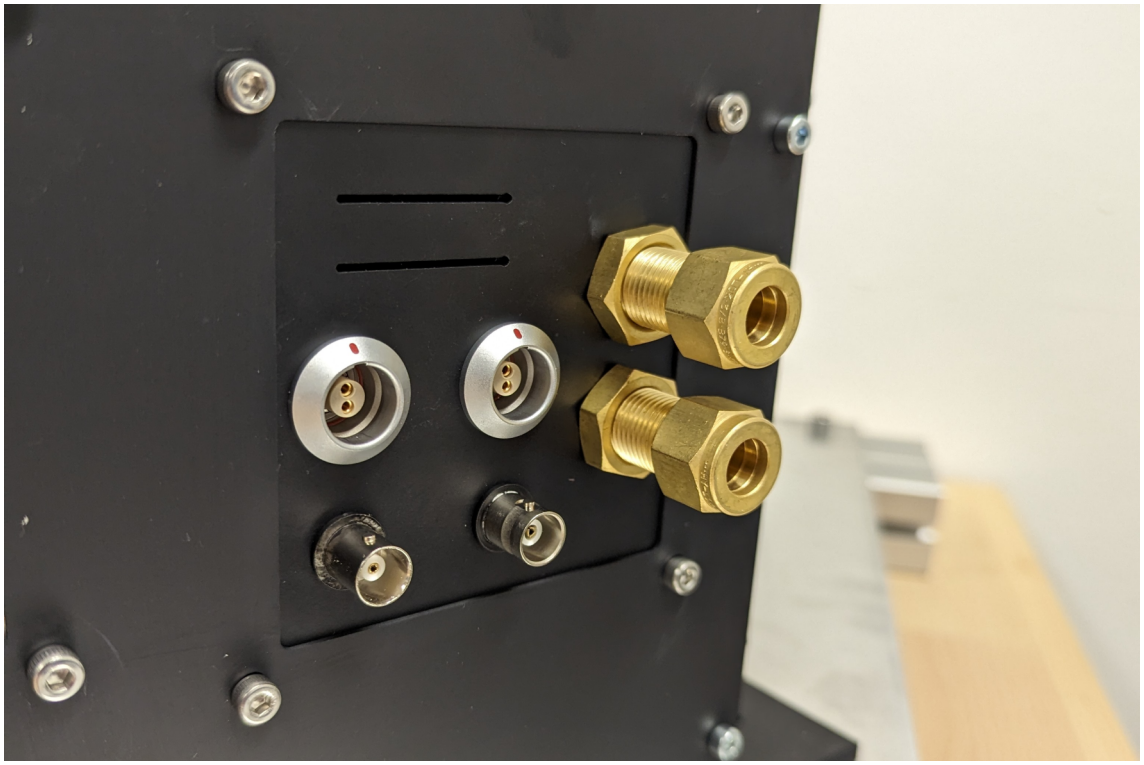

Figure 2.5: Photograph of passthrough panel for physical and electrical connections into the sensor enclosure. Left, from top to bottom: Two slots for differential ribbon cables, for control and readout of front-end electronics; low voltage power for each sensor side; bias voltage for each sensor side. The upper slot and leftmost electrical connections serve the p side of the sensor, while the lower slot and rightmost connections serve the n side. Right: Fittings for liquid cooling.

the enclosure, all internal hydraulic connections are made using fixed copper pipe, which restricts positioning flexibility at the module level.

The front panel, intended to face the patient, also contains a removable element. The 16 µm aluminum window has a minimal effect on the trajectory of energetic secondary fragments, while still being opaque to optical photons and contributing to the Faraday cage formed by the enclosure. As the thin window, shown in Figure 2.6, is much more fragile than other components of the enclosure, it is designed to be removable and replaceable without disassembling the rest of the setup. The foil window is mounted to a frame, which is then connected to the rest of the setup with externally-accessible screws. The 145 mm × 206 mm size of the window is large enough to accommodate the entire field of view of the tracker in any of the configurable positions.

Cooling of the front-end electronics is accomplished using a commercially-available chiller, the S&A CW-5200, which combines a circulation pump with a refrigeration circuit. The 1.77 kW refrigeration capacity of this unit is more than sufficient to maintain a coolant temperature of 20 °C, as the typical power dissipated in each module is less than 50 W. The cold plates mounted to each module are connected in series, reducing the number of fittings required, and therefore the possible leak points. A series connection also ensures

Figure 2.6: Photograph of foil window, mounted to a support frame. This window may be installed or removed from the front of the enclosure, shown in Figure **??**, without removing any of the covering panels.

the consistent flow of chilled water to each module. A drain valve is incorporated into the loop, outside the enclosure, allowing the distilled water used as coolant to be easily drained for maintenance or configuration changes.

2.3 Commissioning

The design of the control and readout system for the prototype fIVI Range Monitoring System differs significantly from prior setups which have used the same sensors. As only two sensors are present in the prototype system, and the total number of sensors used in even a full-scale clinical system is expected to be small compared to the thousands of sensors required for the STS, a low-cost and compact version of the readout chain was selected. This readout chain facilitates the straightforward standalone operation of a moderate number of sensors, while respecting the constraints associated with placing hardware close to the treatment table.

Another change from the original CBM configuration is to the dynamic range of the readout electronics. As the energy deposit expected in the sensor from a clinical beam is significantly higher than that expected in the STS, a lower gain setting, originally intended for use with gas electron multiplier (GEM) detectors, has been selected. When operating the front-end electronics with GEM detectors, the number of active channels is reduced by 50 %, using only half of the input pads on each ASIC [95]. Therefore, operating all channels in this low-gain regime, connected to silicon sensors, requires careful investigation.

2.3.1 Setup

The front-end electronics for each sensor side consist of eight SMX 2.2 application-specific integrated circuits (ASICs), each with 128 independent readout channels [98]. Eight ASICs are mounted to a single front-end board, to read out the 1024 channels from an individual sensor side [99]. It is the internal registers of these ASICs which require configuration to match the needs of the prototype fIVI Range Monitoring System. For initial testing, only one sensor was active at a time. The front-end boards from both sensor sides were connected to a single readout board through an AC-coupled ribbon cable, containing 18 differential pairs: one clock, one downlink for providing commands, and 16 uplinks for receiving data. In initial tests, the clock operated at the full 160 MHz rate, restricting data collection to 14 of the 16 physical uplinks, and 7 of the 8 SMX ASICs, due to the bandwidth of the readout board [100]. The readout board was connected to the control and data acquisition PC through a bidirectional optical link, which transmitted

commands downstream to both the readout board and the front-end electronics, as well as relaying acquired data to the PC. A more complete description of the data acquisition hardware, including the topology when multiple sensors are connected, may be found in Section ??.

The SMX 2.2 ASIC, pictured in Figure 2.7, consists of 128 identical readout channels, along with two test channels which cannot be connected to a sensor. Data processing follows the same process for each channel, without any communication between channels. The incident pulse, originating either from the sensor or the internal pulse generator of the SMX, enters the charge-sensitive preamplifier. The amplified pulse then passes through a polarity selection circuit, which outputs both an upright and an inverted waveform. In this way, the same ASIC design may be used to read out both the p side and the n side of a sensor, which produce opposite pulse polarity due to the difference in primary charge carriers. However, the ASIC must be properly configured as to whether the incoming pulse

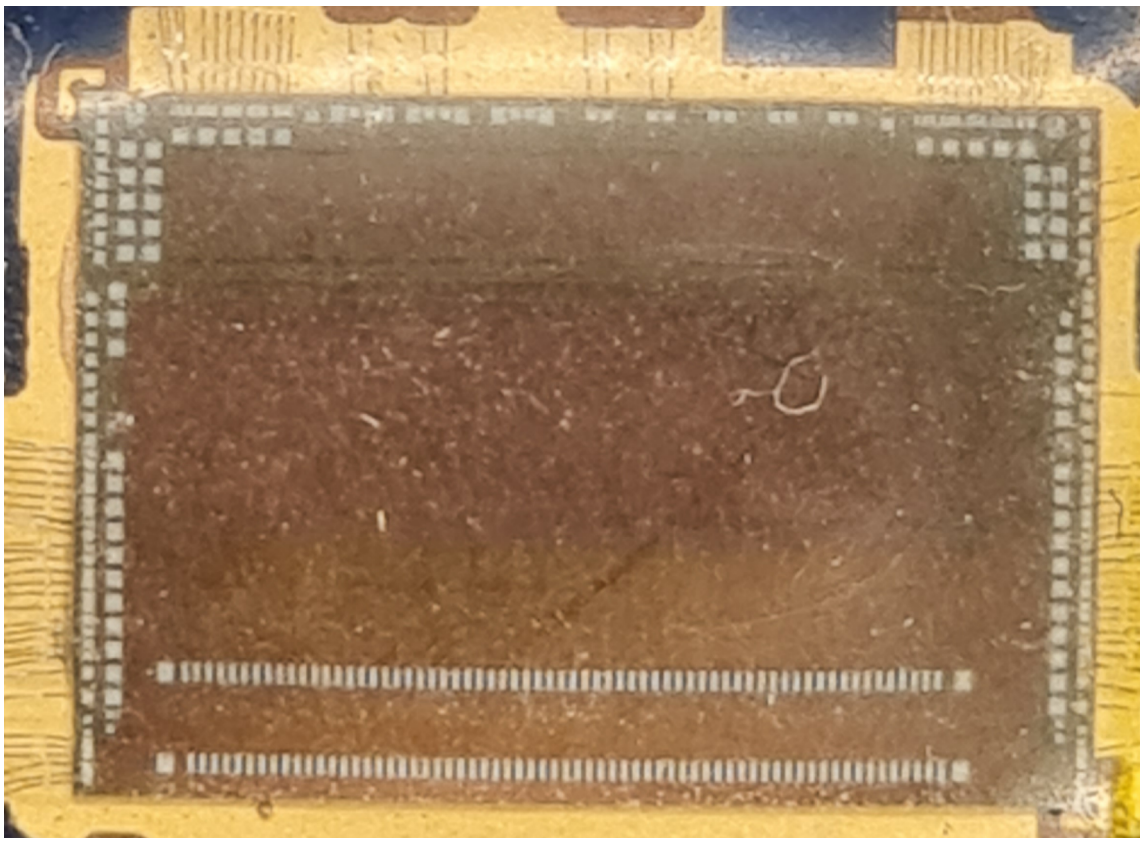

Figure 2.7: Photograph of the 10.0 mm × 6.75 mm SMX 2.2 ASIC, mounted to a front-end circuit board, with wire bonds to the integrated circuit at the top and on either side. Visible at the bottom of the chip are two rows of contacts with a 116 µm pitch; these contacts are connected to the channels of a sensor through analog microcables. Separate cables are used for each row of 64 contacts, leading to slight differences in the performance of even-numbered and odd-numbered channels. In addition to silicon sensors, this ASIC is also designed to read out GEM detectors; in this case, only a single row of inputs is used.

is upright or inverted. The upright output from the polarity selection circuit is passed to a shaper with a short (30 ns) integration time [98]. The purpose of this circuit is to generate a timing signal when an interaction occurs in the sensor. The threshold energy which must be reached in order to latch a timestamp for the interaction is a configurable parameter for each ASIC, with the possibility to apply fine adjustments to each individual channel, to correct for variations in discriminator properties.

The inverted output from the polarity selection circuit is passed to a second shaper with a longer shaping time. The exact time constant is configurable; as the primary consideration for IVI is the rate performance of the system, the shortest shaping time of 90 ns is selected [98]. The output signal from this slow shaper passes through a series of 31 discriminators, with ordered thresholds set by a voltage divider. The number of discriminator thresholds which an individual pulse crosses is encoded as the 5-bit energy of the interaction, acting as an analog-to-digital converter (ADC). This energy is packaged, along with the timestamp from the fast shaper, to provide a full description of the interaction in this channel. As the ADC is more complex than the single discriminator of the timing circuit, more configuration is required. The limits of the ADC, along with the baseline potential, are set for the entire ASIC. However, to accommodate for inter-channel variation and to allow nonlinear energy calibrations, each individual discriminator threshold may be adjusted on a per-channel basis.

The power supply requirements for the detector and readout electronics are rather complex. Each sensor is biased symmetrically, requiring two channels per sensor with opposite polarity. Delivering the bias voltage symmetrically improves the safety of the setup, by minimizing the maximum potential difference to ground. However, this increased safety comes at the cost of requiring a second power supply channel per sensor. Biasing was provided by the CAEN N1471 four-channel supply, with two channels configured to deliver a positive potential relative to ground, and the other two channels configured to deliver a negative potential. In this way, the single power supply was able to bias both sensors in the prototype system, with a ground point allocated on each module, and connected directly to the tracker enclosure.

In addition to bias voltage, each sensor requires multiple low voltage supplies for the front-end electronics. For each sensor side, the low voltage supply is required to float on top of the bias voltage, as the entire readout is operated with its reference at the bias supply [101]. This requirement highlights another benefit of the symmetric biasing of each sensor, as the isolation requirements for the low voltage supply are reduced when the bias voltage is maintained closer to the common ground. As each sensor side sits at a different potential, the supplies for each set of front-end electronics cannot be combined. Each front-end electronics board is designed to accept two low voltage channels per sensor side,

one to supply the analog part of the integrated circuit, and another to supply the digital part. However, as additional voltage regulation takes place directly on the front-end board, for local distribution of the two supply voltages to each SMX, this setup uses a single 3.000 V supply which is connected to both voltage regulators. No performance or noise difference is observed when joining or separating these low voltage channels. Low voltage power was provided by the Rohde and Schwarz HMP 4040 4-channel supply.

Further low-voltage power was required for the readout boards. As their connection to the front-end electronics was AC-coupled, the power supply for these boards was not required to be floating. However, for improved noise performance, the ground plane of each readout board was connected to the common ground point on the tracker enclosure. Power was provided to each readout board directly from the Wiener UEP-20 crate which also contained the bias supply. To reduce the possibility of crosstalk, readout board power was supplied directly from the 24 V rail, which was not used by the bias supply. A schematic of the data and electrical connections within each module and its associated readout board is shown in Figure 2.8.

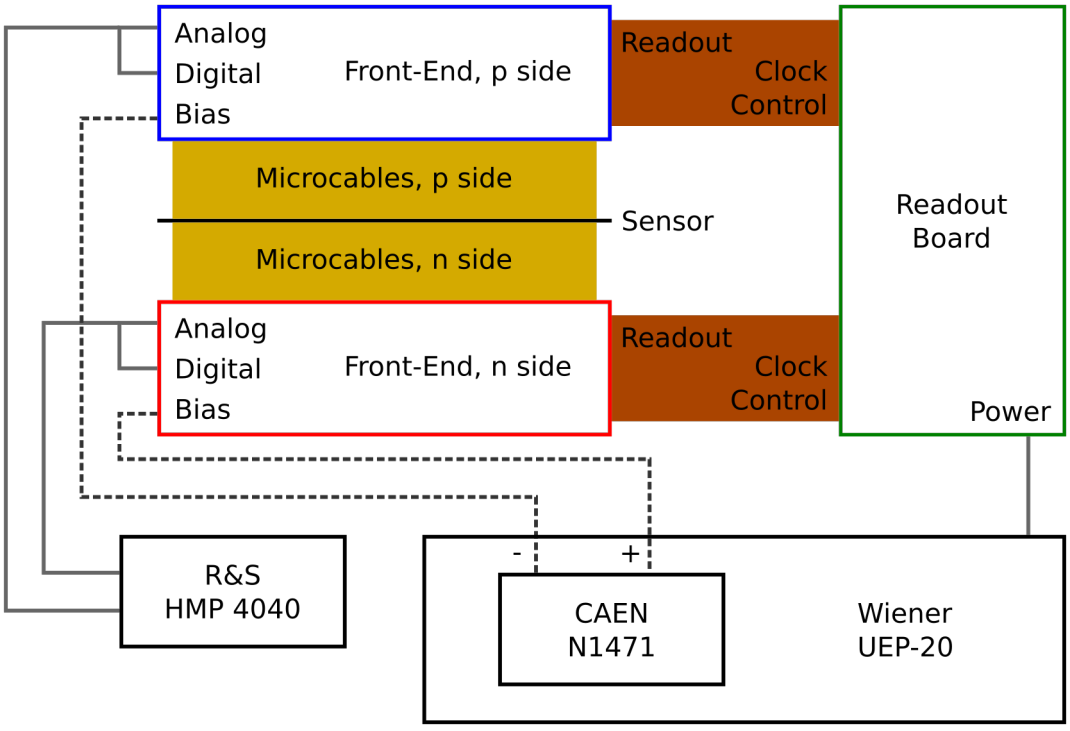

Figure 2.8: Schematic of original module power supply scheme. Low-voltage (grey), bias (black, dashed) and electrical (yellow, brown) connections are shown for a single sensor module. A bias of ±75 V is applied, for a total potential difference of 150 V across the pn junction.

2.3.2 Configuration Tests

The first stage of configuration was to validate the control and readout capability of the system, to ensure that the SMXs could be configured properly to operate in the required combination of gain and active channels, and that data could be recorded. To accomplish these goals, three types of testing were performed. In the first test, configuration values were written to an ASIC by control software, then values were read back from hardware and compared to those written. In the second test, after configuring the ASIC, data acquisition was initiated for a brief period, on the order of seconds. No stimulus was given to the sensor during the acquisition, only a background was collected. The third test was very similar to the second, with the addition of charge injection into each channel of the ASIC through use of the internal test pulse generator of the SMX. This pulse generator produced 100 input signals per channel, with shapes similar to the interaction of an energetic charged particle.

For all configuration tests, the expected values were correctly written to hardware, as confirmed by read requests to individual registers of the SMX. However, the data acquisition performance was significantly worse than expected. Although data was correctly collected by the acquisition system, the noise level was significantly higher than expected, as seen in Figure 2.9. The observed noise level was proportional to the

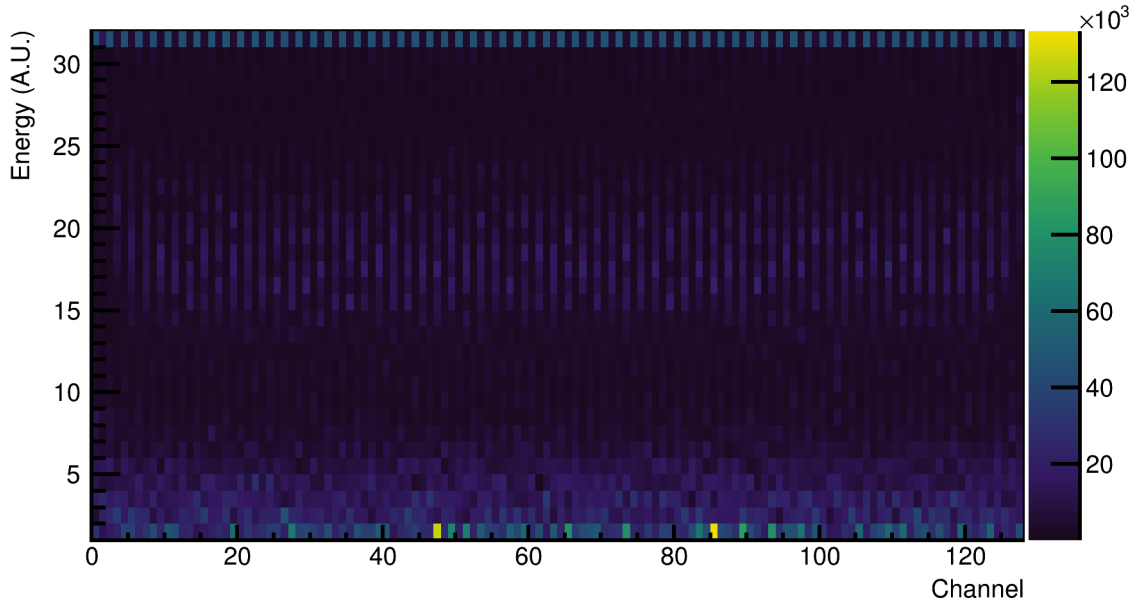

Figure 2.9: Noise performance using the original power supply scheme. Noise events are depicted as a function of channel number for a single SMX on the p side of the 6 cm module. The presented data corresponds to the low-gain mode of operation. The vertical axis shows the entire energy range of the system, with the highest bin containing events which exceed the upper limit of the ADC.

amplifier gain setting, indicating that the observed behaviour was not related to the use of all 128 ASIC channels in the low-gain regime, but due to some other problem with the configuration.

To isolate the problematic setting, a series of tests were conducted with settings and trigger thresholds known to be capable of achieving a low noise level with other sensors. In addition to the variations in ASIC configuration, all power supply hardware was substituted for higher-performance options, to rule out noise caused by input ripple. In this temporary configuration, the sensor bias voltage was supplied by a pair of Keithley 2410 voltage sources, the low voltage supply for the front-end electronics was the Wiener MPV 8016, and the readout board was supplied by the aforementioned Rohde and Schwarz HMP4040.

Repeating background measurements with the updated power supply hardware led to a significant reduction in the noise level, as seen in Figure 2.10. With the lower noise level, a significant difference was also revealed between the two sensors, with the smaller 6 cm tall sensor having a significantly higher noise level than the 12 cm tall sensor, even when a higher threshold was applied to the smaller sensor. The cause of this discrepancy was revealed to be a missing electrical connection between the two sets of front-end electronics which read out the two sides of the more noisy 6 cm sensor. Making this connection yielded an immediate, significant improvement in the noise level. This reduction in noise level is observable in Figure 2.11.

2.3.3 Calibration

Based on the results of the configuration tests, the front-end power supply was replaced with a CAEN A2551A module, which provides improved voltage ripple suppression relative to the HMP4040. With this replacement, the HMP4040 is now permanently assigned to power the readout boards. An updated diagram of the power supply scheme for a single module is shown in Figure 2.12; the noise performance of this configuration in the low-gain mode is indistinguishable from that in Figure 2.10. All further tests and commissioning experiments were completed using this updated power supply scheme.

A final change from the CBM configuration is the use of a slower clock rate for the front-end electronics, reduced from 160 MHz to 80 MHz [102]. While this reduction in clock rate does directly correspond to a reduction in readout rate, it also allows for a more purposeful allocation of the fixed bandwidth of the optical link throughout the detection system by providing support for twice the number of discrete communication links per readout board, increasing from 14 to 28. At the reduced clock rate, a single readout board

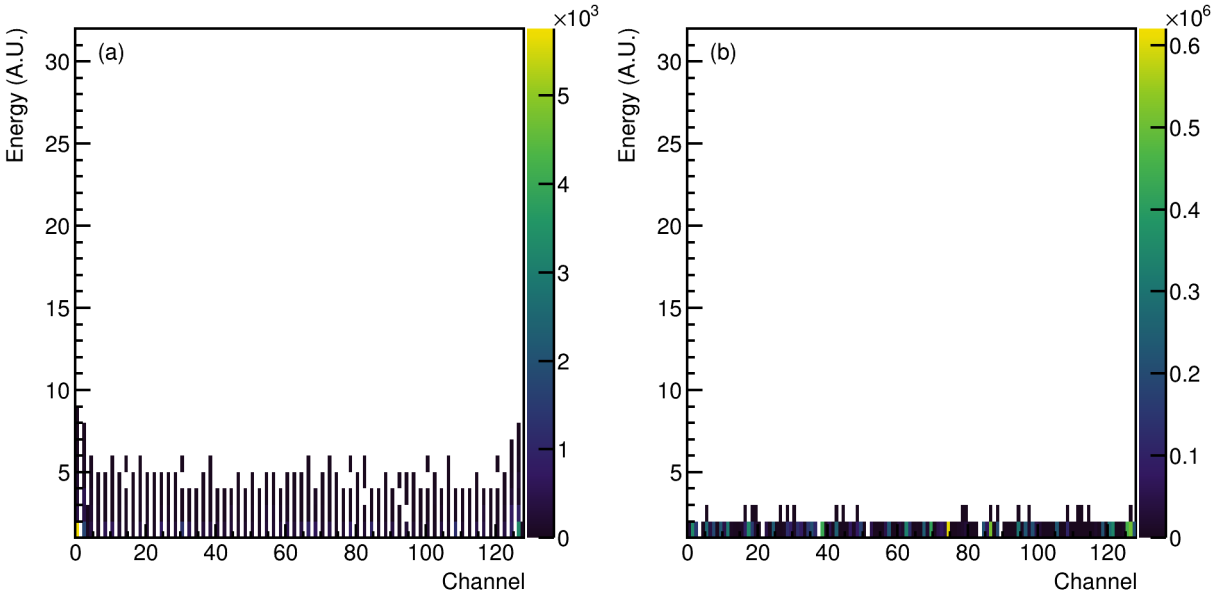

Figure 2.10: Comparison of noise performance between the 6 cm and 12 cm modules. Noise is depicted as a function of channel number for a single SMX on the p side of (a) the 6 cm sensor, and (b) the 12 cm sensor. The presented data corresponds to the low-gain mode of operation, using the Wiener MPV 8016 low-voltage power supply. The noise level is higher on the 6 cm sensor, despite the use of a higher threshold, due to a missing connection between the front-end electronics on opposite sides of the sensor.

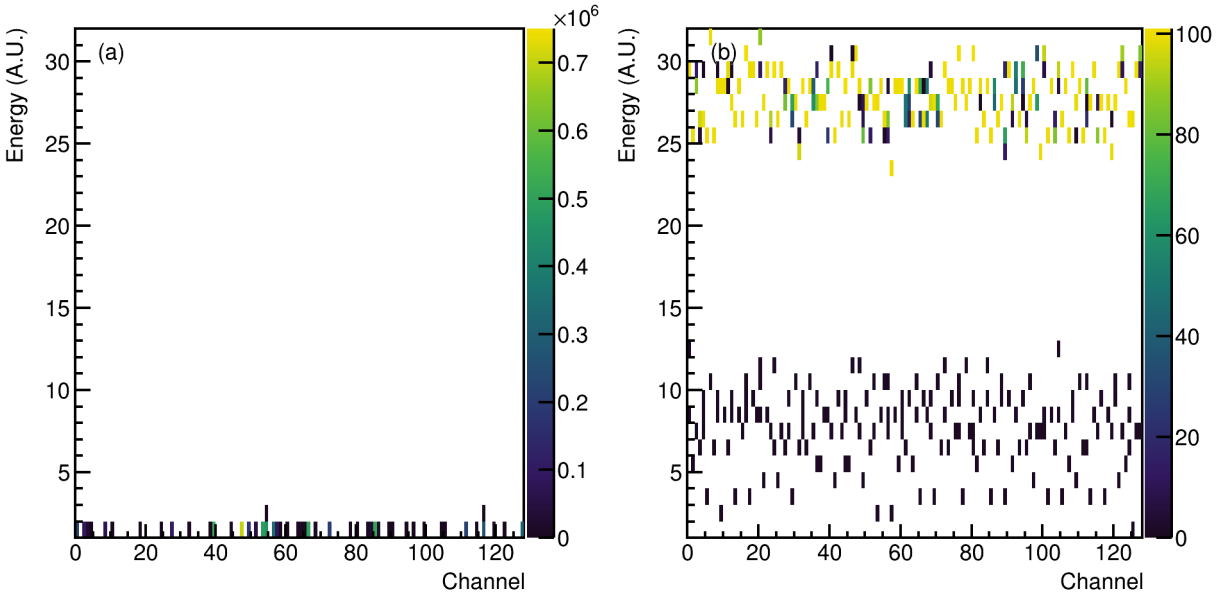

Figure 2.11: Noise performance of the 6 cm module with the front-end electronics joined. Low-voltage power is provided by the CAEN A2551A module. (a) Noise as a function of channel for a single SMX on the p side of the sensor, using a lower threshold than in Figure 2.10a. (b) Channel readout for a single SMX on the p side of the sensor. 100 high-energy pulses have been sent through each channel. The counts at low energy are artifacts produced by activating the pulse generation circuit.

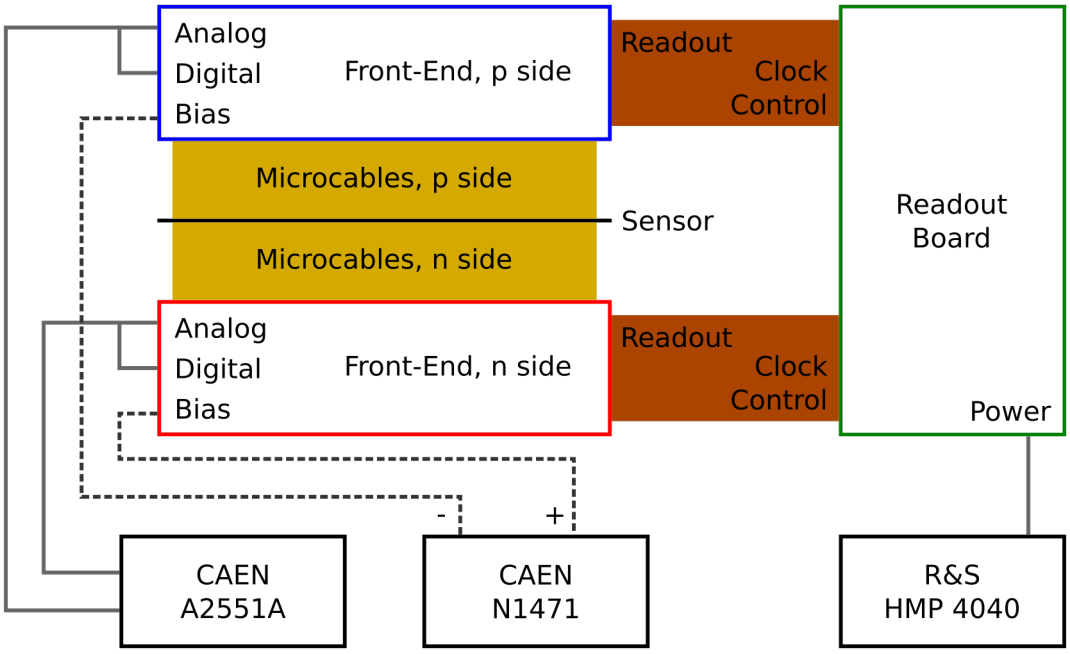

Figure 2.12: Schematic of updated module power supply scheme. Low-voltage (grey), bias (black, dashed) and electrical (yellow, brown) connections are shown for a single sensor module, now using the updated CANE A2551 low-voltage supply. In this scheme, the sensor is now biased at ±70 V, for a total potential difference of 140 V across the pn junction.

is capable of reading out both sides of the same sensor using 16 links, with the remaining 12 links able to be allocated to regions of the sensor which experience higher event rates. However, as the data rate is low during calibration measurements, only a single link per SMX is required, with all other links being disabled.

To prepare each sensor for the collection of experimental data, calibration of the thresholds for both the timing trigger and the analog-to-digital converter for energy measurement are required [103]. While the calibration values are different for each channel, ASIC, and sensor, and are affected by other configuration values, the same calibration is expected to remain valid for a variety of external conditions.

The first stage of calibration is to set the ASIC-wide parameters which define the threshold for the fast discriminator and the ADC limits for energy measurement. For each of these 6-bit values, a target 8-bit pulse amplitude is set for the internal pulse generator, for which 50 % of signals should pass the threshold. Values are varied, using the smallest possible step size, until the proportion of events over the threshold exceeds 50 %. Each parameter is evaluated for 100 test pulses at the specified amplitude, in each of the four central channels of the ASIC. The four central channels are chosen, as the edge channels are most likely to have high noise levels due to correspondence to the edge of a microcable

connecting the sensor to the ASIC. Similarly, an even number of channels are selected in order to represent both even-numbered and odd-numbered channels equally, as these two groups of channels also use different microcables and a different set of input pads on the SMX, often leading to different noise levels. The baseline potential is set at the same value for all ASICs connected to a sensor. A higher baseline is required for the larger sensor, due to higher noise levels associated with longer segments. No scan is performed to evaluate this baseline; the determination of an appropriate value is made based on the results of the complete calibration, in an iterative process. For the 6 cm sensor, a threshold value of 40 was selected, while for the 12 cm sensor, a higher value of 45 was required.

The second stage of calibration is to evaluate the per-channel, per-discriminator fine adjustment values. The algorithm is similar to that used for the ASIC-wide parameters, repeated independently for each discriminator and channel. The fine adjustment is a 6-bit value for the fast discriminator, but an 8-bit value for each ADC discriminator. Therefore, in order to reduce the time required to identify the optimal value for each ADC discriminator, an initial coarse scan is conducted which evaluates every fifth value, to identify the region of values where the 50 % threshold is likely to be found. Then, a fine scan which evaluates every possible adjustment value is conducted only in this region. The number of pulses delivered at each setting also differs from the ASIC-wide scan: for the fast discriminator, 111 test pulses are delivered at each setting, while for the ADC discriminators, 50 test pulses are delivered at each setting, for both the coarse and fine scans. A single target pulse amplitude is set for the fast discriminator across all ASICs, while a linear interpolation between the target amplitudes for first and last discriminators are used to assign targets for each ADC discriminator.

The full calibration process requires approximately four minutes to calibrate each ASIC, or just over one hour for an entire module. After calibration, good agreement is observed between all discriminators with the same target pulse amplitude for a given ASIC, as shown in Figure 2.13. However, small variations do exist between ASICs, which is attributable to different per-ASIC settings, or perhaps different behaviour of the pulse generators integrated into each SMX. For applications where energy resolution is of high importance, additional calibrations could be performed using particles depositing a known energy, to map the raw 5-bit value to a physical energy deposit. However, as discussed in Section 2.1.2, energy resolution is not a high priority for IVI applications, and this degree of inaccuracy may be accepted.

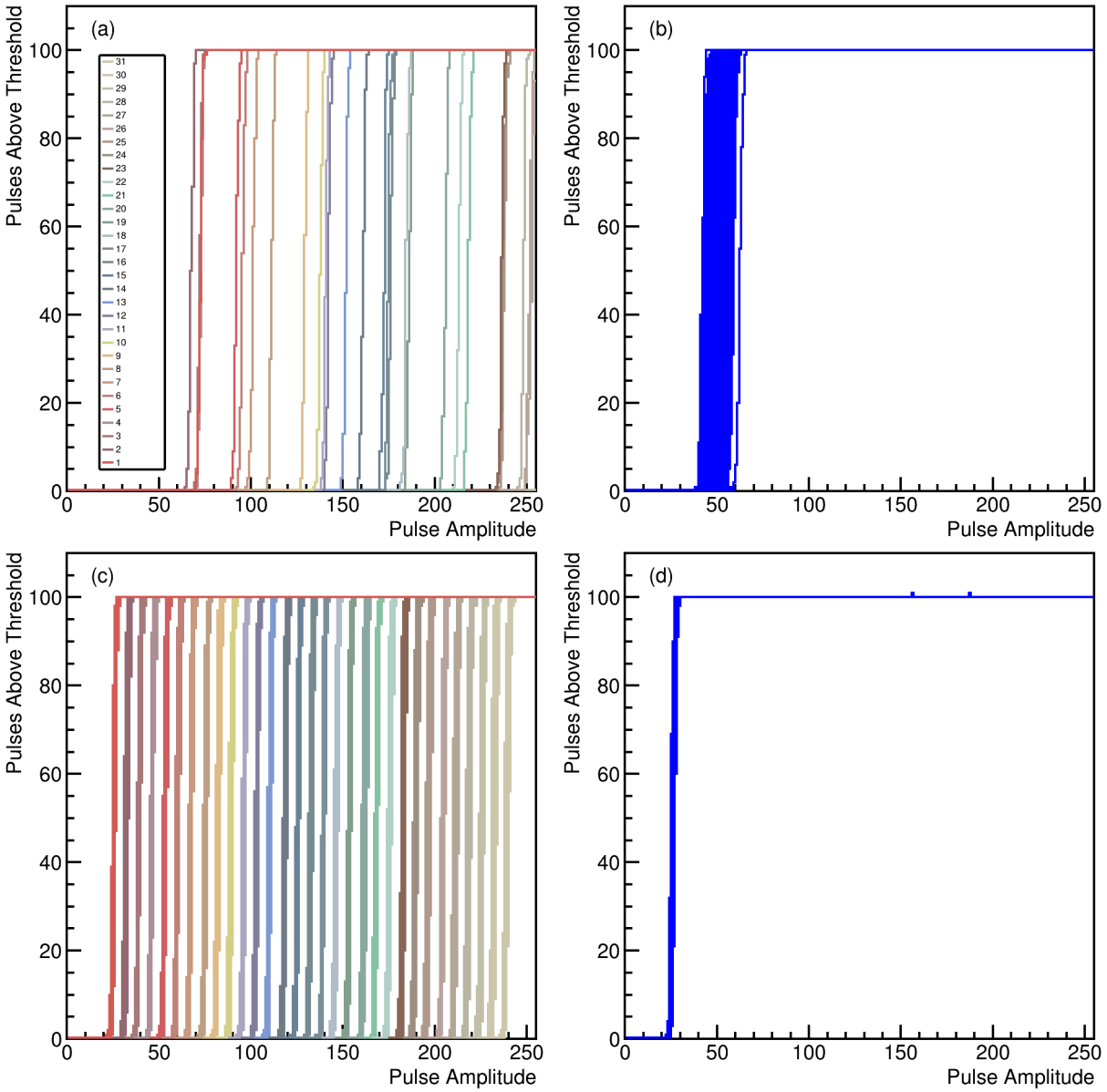

Figure 2.13: Results of discriminator calibration. Depicted are the pre-calibration (a), (b), and post-calibration (c),(d) discriminator response functions for the ADC discriminators (a), (c) and timing discriminator (b), (d). (a) Prior to calibration, the ADC disciminators are unordered, as shown for a single ADC channel. (b) There is significant channel-to-channel variation in the threshold of the timing discriminator; similar variations exist for each ADC discriminator. (c) After calibration, all ADC discriminators on the ASIC are strictly ordered and consistent. The same ordering between discriminator IDs is achieved for all channels; this outcome is vital to proper operation of the ADC. (d) The same consistency is applied to the timing discriminator.

2.3.4 Source Tests

Following calibration, the next goal was to collect data which could be used to validate the response of different segments. For this purpose, a mask was manufactured which mounted directly to the module frame, as shown in Figure 2.14, and could hold a ^{90}Sr β^- source in any of nine positions. These positions corresponded to the nominal centre of the sensor in the module (the same position for both sensors) and to a 4.0 mm inset from the nominal corners of the sensor, for both the 60 mm and 120 mm length. The source was collimated by a 0.6 mm diameter hole through the 5.0 mm thick mask. The near surface of the mask was separated from the sensor surface by 18.5 mm. The total source-to-sensor distance, including the thickness of the mask, was approximately 28.5 mm.

Data were collected for the $60 \times 60\,\text{mm}^2$ sensor in the five central positions, and for the $60 \times 120\,\text{mm}^2$ sensor in all nine positions. Each irradiation lasted for 300 s, using a 1.03 MBq ^{90}Sr source, in equilibrium with its ^{90}Y daughter. Measurements were conducted in air, with the sensor symmetrically biased at ± 70 V, for a total bias voltage of 140 V. Due to the size of the source and alignment mask, only one module at a time was mounted in the enclosure for these tests.

The collected data were processed to reconstruct interaction positions in the plane of the sensor using the process described in Section **??**. For each data set, the reconstructed location of the source, shown in Figure 2.15, is in the appropriate quadrant of the sensor.

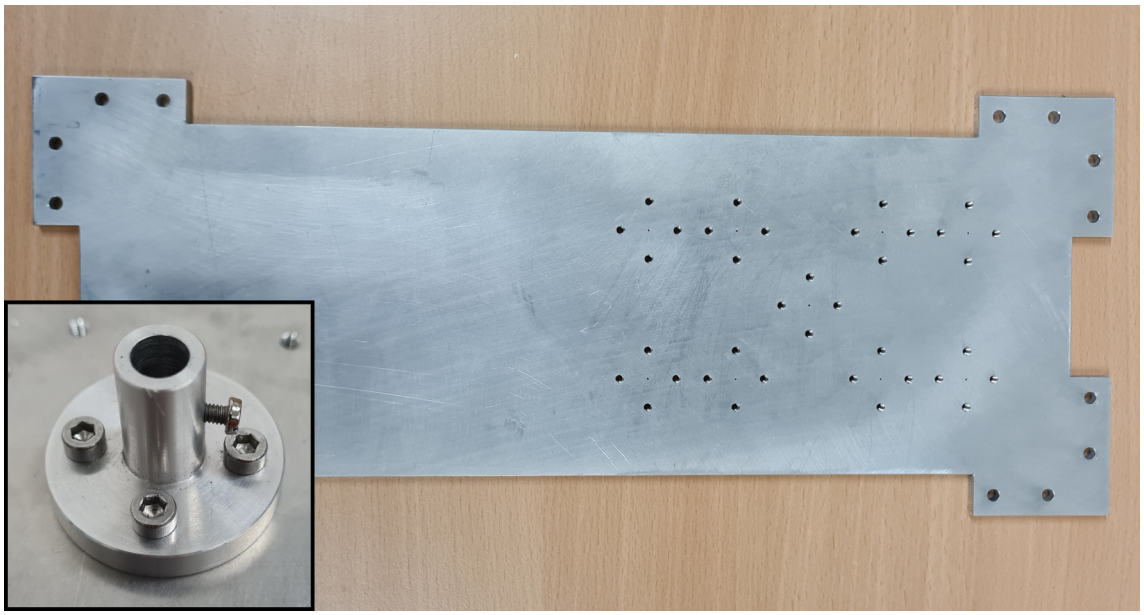

Figure 2.14: Photograph of alignment mask, which may be mounted to the front frame of a module using the holes in each corner. The pictured source holder (inset) may be installed in any of the nine positions.

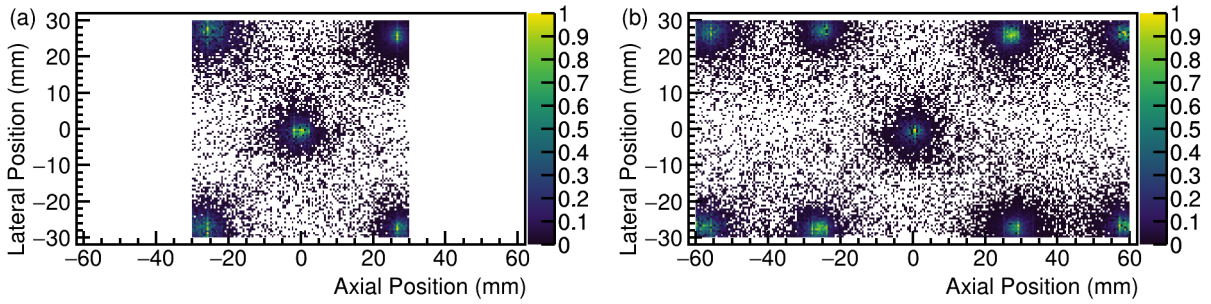

Figure 2.15: Cumulative interaction positions for all source tests on (a) the 6 cm module, and (b) the 12 cm module. Each source position was collected separately for 300 s; the data from each position has been normalized and merged into a single plot.

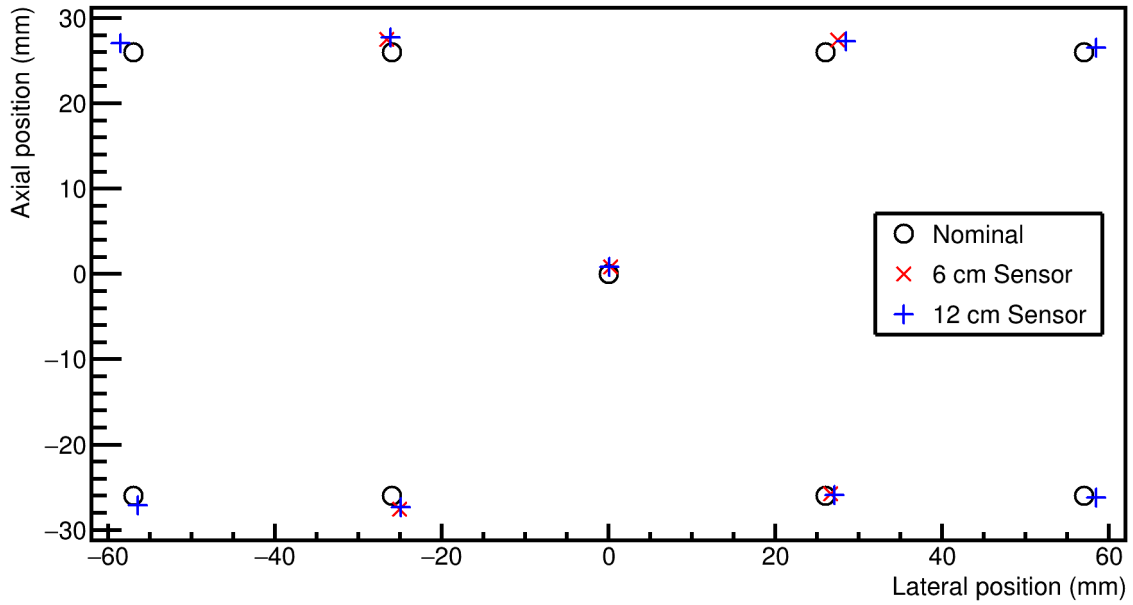

Figure 2.16: Correlation between the measured average interaction position on each module, and the nominal position on the alignment mask, for each source position. The similarity between both modules, and the discrepancy from the nominal position, is explained by a manufacturing inaccuracy affecting the position of the small collimator holes within the mask.

This result indicates that the correlation between channels, ASICs, and physical segments on the sensor is properly implemented in reconstruction. The broadening of each spot, relative to the 0.6 mm diameter hole in the mask, is attributed to scattering of the beta particles in air between the mask and the sensor.

Furthermore, the two sensors demonstrate a very close agreement in absolute position in the sensor plane for the five central source positions, as shown in Figure 2.16. This agreement indicates that the two sensors have been mounted onto their individual backplates and modules in a consistent manner. However, these reconstructed source positions do not match the nominal values expected from construction of the alignment mask. It is believed that this disagreement stems from the manufacture of the alignment

mask, rather than a dramatic and similar systematic error in the positioning of both sensors. Measurements of the alignment mask indicate deviations in the spacing between collimator holes on the order of 1 mm relative to the design, which is sufficient to explain these observations.

2.4 Summary

The sensors selected for the prototype fIVI Range Monitoring System provide excellent intrinsic spatial and timing resolution, in combination with large sensitive areas. The associated readout system is capable of operating at high data rates while remaining compact, minimizing the space required in the treatment room. Further reduction of this space requirement is possible through a future design which may bring the front-end electronics closer to the sensor, reducing the size of a module. The readout system has been successfully adapted to the high dynamic range required for monitoring charged particles at clinically-relevant energies, and demonstrates a low noise level under these circumstances. The prototype fIVI Range Monitoring System is therefore prepared for evaluation under clinically-relevant circumstances, including high beam energies and intensities.

3 Evaluation of a large-area double-sided silicon strip detector for quality assurance in ion-beam radiotherapy

This chapter consists primarily of a manuscript now available at `https://doi.org/10.48550/arXiv.2512.16789`. It describes the first subclinical beam tests of the prototype fIVI Range Monitoring system, which provided evidence that the system, as configured, exceeds the requirements for range monitoring at clinical beam energies and intensities. A summary of the contributions of various authors to this manuscript at the time of thesis submission is as follows:

- O. Bertini, J. Heuser, J. Lehnert, and C. J. Schmidt provided the sensor and readout electronics
- D. Hymers, S. Schroeder, J. Lehnert, and C. J. Schmidt commissioned the setup
- D. Hymers, S. Schroeder, and D. Mücher planned and carried out the low-energy test
- D. Hymers, S. Schroeder, and D. Mücher planned and carried out the clinical beam test
- D. Hymers developed the Monte Carlo simulation
- D. Hymers and S. Schroeder performed Monte Carlo simulations and analyzed the resultant data
- D. Hymers conceptualized and performed the analysis of experimental data
- D. Hymers wrote the manuscript

4 Clinical beam test of inter- and intra-fraction relative range monitoring in carbon ion radiotherapy

This chapter consists primarily of a manuscript now available at `https://doi.org/10.48550/arXiv.2512.16798`. It describes the first test of the fIVI Range Monitoring System which combined clinically-relevant beams and human-sized plastic phantoms, and evaluated the relative range monitoring performance. A summary of the contributions of various authors to this manuscript at the time of thesis submission is as follows:

- O. Bertini, J. Heuser, J. Lehnert, and C. J. Schmidt provided the sensor and readout electronics
- D. Hymers, S. Schroeder, J. Lehnert, and C. J. Schmidt commissioned the setup
- D. Hymers, S. Schroeder, S. Brons, and D. Mücher planned and carried out the experiment
- D. Hymers conceptualized and performed the analysis of experimental data
- D. Hymers wrote the manuscript

5 A parallel, pipeline-based online analysis system for Interaction Vertex Imaging

This chapter consists primarily of a manuscript now available at `https://doi.org/10.48550/arXiv.2512.16800`. It describes the design and evaluation of a high-performance analysis system for fIVI, which is intended to be run concurrently with primary data acquisition. The post-irradiation time required to make a range shift determination is compared to timescales relevant to beam delivery. A summary of the contributions of various authors to this manuscript at the time of thesis submission is as follows:

- O. Bertini, J. Heuser, J. Lehnert, and C. J. Schmidt provided the sensor and readout electronics
- D. Hymers and D. Mücher conceptualized the analysis algorithm
- D. Hymers and S. Schroeder developed the control software
- D. Hymers developed the readout software
- D. Hymers developed the analysis software
- D. Hymers collected the performance data
- D. Hymers conceptualized and performed the analysis of performance
- D. Hymers wrote the manuscript

6 Summary and Conclusion

This thesis describes the commissioning and initial test results of a first-of-its-kind system using double-sided strip-segmented silicon detectors, developed for online range monitoring in carbon ion radiotherapy using the filtered Interaction Vertex Imaging method. The sensors and readout electronics are successfully adapted to the use of all readout channels in a low-gain operation mode. The use of this low-gain mode expands the dynamic range of the sensors to accept the high energy deposit typical when monitoring clinical $^{12}C^{6+}$ beams with energy on the order of 100 MeV u^{-1}. This system demonstrates excellent spatial resolution, due to the fine segmentation of the sensors, along with a low noise floor facilitated by the use of a low-ripple power supply for the front-end electronics.

The suitability of this system to operation at the high data rates demanded by clinical irradiation, on the order of MHz per sensor, has been definitively established. Even at these high rates, the fraction of events lost due to pileup or dead time is negligible, and the efficiency of the system at reconstructing interactions and tracking particles approaches 100 %, indicating that monitoring of clinical irradiation is well within the capabilities of this device. This high performance extends to monitoring and reconstruction at clinical beam energies, with the higher momentum of a clinical beam correlating to improved tracking performance, as the influence of scattering in air is significantly reduced at clinically-relevant beam energies as compared to 19 MeV protons.

The irradiation of a 16 cm diameter homogeneous plastic phantom modelled the treatment of a tumour in the head, or in a pediatric patient. In this model, the system was able to differentiate between Bragg peak positions separated by as little as 800 µm, although full consistency was only achieved at greater than clinical statistics. The system demonstrates millimetric precision (1σ) at clinically-relevant statistics of 10^7 primary ions per BP, and extends this precision to Bragg peak depths as low as 50 mm. Repeating the procedure with a 32 cm diameter phantom representative of the adult torso results in significantly lower precision, and an impaired ability to perform RM at clinical doses. Millimetric precision is only achieved with doses an order of magnitude above clinical. Further increases to the sensitive area of the detection system would be required to enable IVI RM for deep tumours in large areas of the body.

Online analysis of this clinically-relevant data, modelled by replaying the data collected in plastic phantoms at the rate it was originally acquired, has been demonstrated to

complete a range shift determination less than 200 ms after the end of irradiation. This window is short enough to allow evaluation of the accuracy of each beam before the next energy step is delivered, being comparable to the time required to change energy in a synchrotron accelerator. This performance is sufficient to allow the incorporation of fIVI into online safety and quality assurance mechanisms of the beam delivery system, pausing or aborting a treatment if unacceptably-large deviations in beam range are detected.

The overall millimetric performance of the prototype fIVI Range Monitoring System matches other range monitoring approaches used in carbon ion radiotherapy, particularly in the head and neck, and extends this precision to the challenging case of shallow BP positions [54, 56, 60]. The addition of a high-performance online analysis system allows processing of each individual beam to complete before the next is delivered, placing only minor limitations on the treatment system [104]. The observed headroom in rate performance of the analysis system invites an investigation of the possibility of monitoring FLASH irradiation with this system. As FLASH treatments must be delivered in a single synchrotron spill, without pausing, the benefits of the online analysis system would not apply to this use case [105]. However, as FLASH treatments are still often fractionated [24], inter-fraction range monitoring with IVI would still be possible, providing the benefits of quality assurance to each fraction.

A key challenge in IVI is the collection of sufficient statistics to achieve high precision at clinically-relevant spot intensities between 10^4 and 10^7 primary ions per fraction [7, 62]. The use of large and high-rate-capable sensors facilitates the straightforward implementation of optimizations to sensor positioning and overall sensitive area, which are expected to directly translate into an improvement in range monitoring precision. The excellent high-rate performance and flexible data acquisition hardware support a variety of improvements to the system, such as increasing the tracker acceptance through adding an additional sensor to the rear layer, thereby doubling the sensitive area.

Optimization remains to be performed regarding the optimal positioning, particularly the off-axis angle, of the fIVI Range Monitoring System relative to the patient. While a greater number of secondary fragments are produced at smaller angles, the inherent spatial resolution of these fragments is reduced, for geometric reasons [106]. The optimal positioning of the device (i.e. that which provides the highest precision) is known from prior studies to differ based on sensor geometry, and may also be affected by the geometry of the patient and tumour, such as through an effect of the typical path length of fragments as they travel toward the sensors [60, 73]. Although operating the fIVI Range Monitoring System at a smaller off-axis angle will increase the count rate requirements, the high-rate sensors and performant online analysis system allow full flexibility in positioning, to best suit the needs of the clinical environment.

Particularly in the case of abdominal tumours, or use cases demanding robust intra-fraction monitoring, precision improvements may be achieved through increasing the total sensitive area. This increase could be achieved either through the addition of more independent trackers, or through a larger sensor array placed at a single location. An increase in the overall volume of the tracker would be in line with other devices used for IVI; furthermore, the design of these strip-segmented sensors makes them particularly well-suited for a system in which a high fraction of the total tracker area is made sensitive [56, 61]. The resultant improvement in collectable statistics is expected to provide both an improvement in RM performance, as well as an increase in the proportion of beams which can be monitored with maximum precision.

Due to the parallel architecture of the analysis system, increasing the number of sensors in this way is not anticipated to have a significant impact on the performance of online analysis. As the most expensive portions of analysis demonstrate the greatest opportunity for additional parallelism, the demands of an increased number of sensors may be addressed entirely by an increase in the number of parallel tasks. While the current two-sensor setup was processed on a workstation with only 24 physical CPU cores, machines are commercially available with up to 386 physical cores. As the current primary limitation in performance has been observed to be contention in an oversubscribed system, further performance improvements may also be achieved for the existing setup through such an increase in processing capacity. Further improvements may also be possible by shifting some portions of the analysis to dedicated hardware, such as processing timestamps on the readout electronics, or taking advantage of coprocessors or graphics processing units to accelerate certain parallel tasks.

Overall, the prototype fIVI Range Monitoring System has clearly demonstrated its capability for online range monitoring. This system, the first to utilize large-area silicon sensors, is able to perform online quality assurance of high-intensity spots delivered at a wide variety of depths in a head or neck treatment, with a range difference precision of 1.0 mm (1σ). The implementation of online monitoring facilitates safety, by allowing a treatment to be paused or aborted within 200 ms if inter-fraction deviations are detected, with further interlocks possible through intra-fraction monitoring, if spots with sufficient ion intensity exist at different energies. Precision improvements achieved through optimization of the positioning and size of the device are projected to allow a reduction in the safety margin applied during treatment planning, which will directly correspond to a reduction in the amount of irradiated healthy tissue. In this way, the fIVI Range Monitoring System may directly improve the safety of carbon ion radiotherapy, reducing the risk of healthy tissue toxicity and secondary cancer while maintaining a high rate of tumour control.

7 References

1. Roth GA et al. Global, regional, and national age-sex-specific mortality for 282 causes of death in 195 countries and territories, 1980–2017: a systematic analysis for the Global Burden of Disease Study 2017. Lancet 2018; **392**(10159) 1736–88. DOI: 10.1016/S0140-6736(18)32203-7
2. Bray F, Laversanne M, Weiderpass E, and Soerjomataram I. The Ever-Increasing Importance of Cancer as a Leading Cause of Premature Death Worldwide. Cancer 2021; **127**(16) 3029–30. DOI: 10.1002/cncr.33587
3. Bray F, Laversanne M, Sung H, Ferlay J, Siegel RL, Soerjomataram I, and Jemal A. Global cancer statistics 2022: GLOBOCAN estimates of incidence and mortality worldwide for 36 cancers in 185 countries. CA Cancer J. Clin. 2024; **74**(3) 229–63. DOI: 10.3322/caac.21834
4. Delaney GP and Barton MB. Evidence-based Estimates of the Demand for Radiotherapy. Clin. Oncol. 2015; **27**(2) 70–6. DOI: 10.1016/j.clon.2014.10.005
5. Hanahan D. Hallmarks of Cancer: New Dimensions. Cancer Discov. 2022; **12**(1) 31–46. DOI: 10.1158/2159-8290.CD-21-1059
6. Tubiana M. Can we reduce the incidence of second primary malignancies occurring after radiotherapy? A critical review. Radiother. Oncol. 2009; **91**(1) 4–15. DOI: 10.1016/j.radonc.2008.12.016
7. Krämer M, Jäkel O, Haberer T, Kraft G, Schardt D, and Weber U. Treatment planning for heavy-ion radiotherapy: physical beam model and dose optimization. Phys. Med. Biol. 2000; **45**(11) 3299–317. DOI: 10.1088/0031-9155/45/11/313
8. Melia E and Parsons JL. DNA damage and repair dependencies of ionising radiation modalities. Biosci. Rep. 2023; **43**(10) BSR20222586. DOI: 10.1042/BSR20222586
9. Reisz JA, Bansal N, Qian J, Zhao W, and Furdui CM. Effects of Ionizing Radiation on Biological Molecules—Mechanisms of Damage and Emerging Methods of Detection. Antioxid. Redox Sign. 2014; **21**(2) 260–92. DOI: 10.1089/ars.2013.5489
10. Douki T, Ravanat JL, Pouget JP, Testard I, and Cadet J. Minor contribution of direct ionization to DNA base damage induced by heavy ions. Int. J. Radiat. Biol. 2006; **82**(2) 119–27. DOI: 10.1080/09553000600573788

11. Beuve M, Moreau JM, Rodriguez C, and Testa E. Biological systems: from water radiolysis to carbon ion radiotherapy. J. Phys. Conf. Ser. 2015; **629** 012004. DOI: 10.1088/1742-6596/629/1/012004

12. Thompson LH. Recognition, signaling, and repair of DNA double-strand breaks produced by ionizing radiation in mammalian cells: The molecular choreography. Mutat. Res. Rev. Mutat. Res. 2012; **751**(2) 158–246. DOI: 10.1016/j.mrrev.2012.06.002

13. Noda A, Hirai Y, Hamasaki K, Mitani H, Nakamura N, and Kodama Y. Unrepairable DNA double-strand breaks that are generated by ionising radiation determine the fate of normal human cells. J. Cell Sci. 2012; **125**(22) 5280–7. DOI: 10.1242/jcs.101006

14. Tutt A, Connor F, Bertwistle D, Kerr P, Peacock J, Ross G, and Ashworth A. Cell cycle and genetic background dependence of the effect of loss of BRCA2 on ionizing radiation sensitivity. Oncogene 2003; **22**(19) 2926–31. DOI: 10.1038/sj.onc.1206522

15. Klinakis A, Karagiannis D, and Rampias T. Targeting DNA repair in cancer: current state and novel approaches. Cell. Mol. Life Sci. 2019; **77**(4) 677–703. DOI: 10.1007/s00018-019-03299-8

16. Blakely EA, Chang PY, and Lommel L. Cell-Cycle-Dependent Recovery from Heavy-Ion Damage in G_1-Phase Cells. Radiat. Res. 1985; **104**(2) S145–S157. DOI: 10.2307/3576641

17. McBride WH and Schaue D. Radiation-induced tissue damage and response. J. Pathol. 2020; **250**(5) 647–55. DOI: 10.1002/path.5389

18. Scifoni E, Tinganelli W, Weyrather WK, Durante M, Maier A, and Krämer M. Including oxygen enhancement ratio in ion beam treatment planning: model implementation and experimental verification. Phys. Med. Biol. 2013; **58**(11) 3871–95. DOI: 10.1088/0031-9155/58/11/3871

19. Barendsen GW. Dose fractionation, dose rate and iso-effect relationships for normal tissue responses. Int. J. Radiat. Oncol. Biol. Phys. 1982; **8**(11) 1981–97. DOI: 10.1016/0360-3016(82)90459-X

20. McMahon SJ. The linear quadratic model: usage, interpretation and challenges. Phys. Med. Biol. 2019; **64**(1) 01TR01. DOI: 10.1088/1361-6560/aaf26a

21. Williams MV, Denekamp J, and Fowler JF. A review of α/β ratios for experimental tumors: implications for clinical studies of altered fractionation. Int. J. Radiat. Oncol. Biol. Phys. 1985; **11**(1) 87–96. DOI: 10.1016/0360-3016(85)90366-9

22. Fowler JF, Harari PM, Leborgne F, and Leborgne JH. Acute radiation reactions in oral and pharyngeal mucosa: tolerable levels in altered fractionation schedules. Radiother. Oncol. 2003; **69**(2) 161–8. DOI: 10.1016/S0167-8140(03)00231-7

23. Sokol O and Durante M. Carbon Ions for Hypoxic Tumors: Are We Making the Most of Them? Cancers 2023; **15**(18) 4494. DOI: 10.3390/cancers15184494

24. Hughes JR and Parsons JL. FLASH Radiotherapy: Current Knowledge and Future Insights Using Proton-Beam Therapy. Int. J. Mol. Sci. 2020; **21**(18) 6492. DOI: 10.3390/ijms21186492

25. Haberer T, Becher W, Schardt D, and Kraft G. Magnetic scanning system for heavy ion therapy. Nucl. Instrum. Meth. A 1993; **330**(1-2) 296–305. DOI: 10.1016/0168-9002(93)91335-K

26. Madani I, Duprez F, Boterberg T, Van de Wiele C, Bonte K, Deron P, De Gersem W, Coghe M, and De Neve W. Maximum tolerated dose in a phase I trial on adaptive dose painting by numbers for head and neck cancer. Radiother. Oncol. 2011; **101**(3) 351–5. DOI: 10.1016/j.radonc.2011.06.020

27. Matuszak N, Suchorska WM, Milecki P, Kruszyna-Mochalska M, Misiarz A, Pracz J, and Malicki J. FLASH radiotherapy: an emerging approach in radiation therapy. Rep. Pract. Oncol. Radiother. 2022; **27**(2) 343–51. DOI: 10.5603/RPOR.a2022.0038

28. Amaldi U and Braccini S. Present challenges in hadrontherapy techniques. Eur. Phys. J. Plus 2011; **126**(7) 70. DOI: 10.1140/epjp/i2011-11070-4

29. Castro JR, Linstadt DE, Bahary JP, Petti PL, Daftari I, Collier JM, Gutin PH, Gauger G, and Phillips TL. Experience in charged particle irradiation of tumors of the skull base: 1977–1992. Int. J. Radiat. Oncol. Biol. Phys. 1994; **29**(4) 647–55. DOI: 10.1016/0360-3016(94)90550-9

30. Tessonnier T, Mairani A, Brons S, Haberer T, Debus J, and Parodi K. Experimental dosimetric comparison of ^{1}H, ^{4}He, ^{12}C and ^{16}O scanned ion beams. Phys. Med. Biol. 2017; **62**(10) 3958–82. DOI: 10.1088/1361-6560/aa6516

31. Gunzert-Marx K, Iwase H, Schardt D, and Simon RS. Secondary beam fragments produced by 200 MeV u-1 12C ions in water and their dose contributions in carbon ion radiotherapy. New J. Phys. 2008; **10**(7) 075003. DOI: 10.1088/1367-2630/10/7/075003

32. Amaldi U and Kraft G. Radiotherapy with beams of carbon ions. Rep. Prog. Phys. 2005; **68**(8) 1861–82. DOI: 10.1088/0034-4885/68/8/R04

33. Jäkel O, Krämer M, Karger CP, and Debus J. Treatment planning for heavy ion radiotherapy: clinical implementation and application. Phys. Med. Biol. 2001; **46**(4) 1101–16. DOI: 10.1088/0031-9155/46/4/314

34. Kumagai M, Hara R, Mori S, Yanagi T, Asakura H, Kishimoto R, Kato H, Yamada S, Kandatsu S, and Kamada T. Impact of Intrafractional Bowel Gas Movement on Carbon Ion Beam Dose Distribution in Pancreatic Radiotherapy. Int. J. Radiat. Oncol. Biol. Phys. 2009; **73**(4) 1276–81. DOI: 10.1016/j.ijrobp.2008.10.055

35. Eichkorn T, König L, Held T, Naumann P, Harrabi S, Ellerbrock M, Herfarth K, Haberer T, and Debus J. Carbon Ion Radiation Therapy: One Decade of Research and Clinical Experience at Heidelberg Ion Beam Therapy Center. Int. J. Radiat. Oncol. Biol. Phys. 2021; **111**(3) 597–609. DOI: 10.1016/j.ijrobp.2021.05.131

36. Schardt D, Elsässer T, and Schulz-Ertner D. Heavy-ion tumor therapy: Physical and radiobiological benefits. Rev. Mod. Phys. 2010; **82**(1) 383–425. DOI: 10.1103/RevModPhys.82.383

37. Yasuda S, Kato H, Imada H, Isozaki Y, Kasuya G, Makishima H, Tsuji H, Ebner DK, Yamada S, Kamada T, Tsujii H, Kato N, Miyazaki M, Arii S, Ebara M, Furuse J, Ohara K, Okusaka T, Otsubo T, Otsuka M, Kanai F, Kondo F, Saito A, Shimizu Y, Takayasu K, Udagawa I, Yamamoto H, Yamamoto J, Yamamoto M, Yokosuka O, and Yoshidome H. Long-Term Results of High-Dose 2-Fraction Carbon Ion Radiation Therapy for Hepatocellular Carcinoma. Adv. Radiat. Oncol. 2020; **5**(2) 196–203. DOI: 10.1016/j.adro.2019.09.007

38. Byskov CS, Hansen CR, Dahlrot RH, Haldbo-Classen L, Haslund CA, Kjær-Kristoffersen F, Kristensen TO, Lassen-Ramshad Y, Lukacova S, Muhic A, Nyström PW, Weber B, and Kallehauge JF. Treatment plan comparison of proton vs photon radiotherapy for lower-grade gliomas. Phys. Imag. Radiat. Onc. 2021; **20** 98–104. DOI: 10.1016/j.phro.2021.11.008

39. Jang JY, Kim K, Chen MF, Akimoto T, Wang MLC, Kim MJ, Kim K, Lee TH, Yoo GS, and Park HC. A meta-analysis comparing efficacy and safety between proton beam therapy versus carbon ion radiotherapy. Cancer Medicine 2024; **13**(3) e7023. DOI: 10.1002/cam4.7023

40. Laprie A, Hu Y, Alapetite C, Carrie C, Habrand JL, Bolle S, Bondiau PY, Ducassou A, Huchet A, Bertozzi AI, Perel Y, Moyal É, and Balosso J. Paediatric brain tumours: A review of radiotherapy, state of the art and challenges for the future regarding protontherapy and carbontherapy. Cancer Radiother. 2015; **19**(8) 775–89. DOI: 10.1016/j.canrad.2015.05.028

41. Peeters A, Grutters JPC, Pijls-Johannesma M, Reimoser S, De Ruysscher D, Severens JL, Joore MA, and Lambin P. How costly is particle therapy? Cost analysis of external beam radiotherapy with carbon-ions, protons and photons. Radiother. Oncol. 2010; **95**(1) 45–53. DOI: 10.1016/j.radonc.2009.12.002

42. PTCOG - Facilities in Operation (public). Available from: https://ptcog.site/index.php/facilities-in-operation-public [Accessed on: 2025 Mar 12]

43. Haberer T, Debus J, Eickhoff H, Jäkel O, Schulz-Ertner D, and Weber U. The heidelberg ion therapy center. Radiother. Oncol. 2004; **73**(S2) S186–S190. DOI: 10.1016/S0167-8140(04)80046-X

44. Dolinskii A, Eickhoff H, and Franczak B. The Synchrotron of the Dedicated Ion Beam Facility for Cancer Therapy, proposed for the Clinic in Heidelberg. *Proceedings of EPAC 2000*. Vienna, Austria, 2000 2509–11. Available from: accelconf.web.cern.ch/e00/PAPERS/WEP3A12.pdf

45. Schömers C, Feldmeier E, Haberer T, Naumann J, Panse RE, and Peters A. Implementation of an Intensity Feedback-loop for an Ion-therapy Synchrotron. *Proceedings of IPAC 2011*. San Sebastián, Spain, 2011 2851–3. Available from: accelconf.web.cern.ch/IPAC2011/papers/thoaa02.pdf

46. Hoffmann T, Ondreka D, Peters A, Reiter A, and Schwickert M. Beam Quality Measurements at the Synchrotron and HEBT of the Heidelberg Ion Therapy Center. *Proceedings of BIW08*. Lake Tahoe, California, USA, 2008 210–2. Available from: accelconf.web.cern.ch/BIW2008/papers/tuptpf044.pdf

47. Ondreka D and Weinrich U. The Heidelberg Ion Therapy (HIT) Accelerator Coming into Operation. *Proceedings of EPAC08*. Genoa, Italy, 2008 979–81. Available from: accelconf.web.cern.ch/e08/papers/tuocg01.pdf

48. Galonska M, Feldmeier E, Haberer T, Peters A, and Schoemers C. Multi-Energy Trial Operation of the HIT Medical Synchrotron: Accelerator Model and Data Supply. *Proceedings of IPAC2017*. Copenhagen, Denmark, 2017 4644–6. DOI: 10.18429/JACoW-IPAC2017-THPVA082

49. Schwaab J, Brons S, Fieres J, and Parodi K. Experimental characterization of lateral profiles of scanned proton and carbon ion pencil beams for improved beam models in ion therapy treatment planning. Phys. Med. Biol. 2011; **56**(24) 7813–27. DOI: 10.1088/0031-9155/56/24/009

50. Crowe K, Kanstein L, Lyman J, and Yeater F. A Large-Field Medical Beam at the 184-inch synchrocyclotron. Tech. rep. LBL-4235. Lawrence Berkeley Laboratory, 1975. Available from: https://escholarship.org/uc/item/93d4v7dj

51. Chu WT, Ludewigt BA, and Renner TR. Instrumentation for treatment of cancer using proton and light-ion beams. Rev. Sci. Instrum. 1993; **64**(8) 2055–122. DOI: 10.1063/1.1143946

52. Goitein M. Compensation for inhomogeneities in charged particle radiotherapy using computed tomography. Int. J. Radiat. Oncol. Biol. Phys. 1978; **4**(5) 499–508. DOI: 10.1016/0360-3016(78)90087-1

53. Ringbæk TP, Weber U, Santiago A, Simeonov Y, Fritz P, Krämer M, Wittig A, Bassler N, Engenhart-Cabillic R, and Zink K. Dosimetric comparisons of carbon ion treatment plans for 1D and 2D ripple filters with variable thicknesses. Phys. Med. Biol. 2016; **61**(11) 4327–41. DOI: 10.1088/0031-9155/61/11/4327

54. Fischetti M, Baroni G, Battistoni G, Bisogni G, Cerello P, Ciocca M, De Maria P, De Simoni M, Di Lullo B, Donetti M, Dong Y, Embriaco A, Ferrero V, Fiorina E, Franciosini G, Galante F, Kraan A, Luongo C, Magi M, Mancini-Terracciano C, Marafini M, Malekzadeh E, Mattei I, Mazzoni E, Mirabelli R, Mirandola A, Morrocchi M, Muraro S, Patera V, Pennazio F, Schiavi A, Sciubba A, Solfaroli Camillocci E, Sportelli G, Tampellini S, Toppi M, Traini G, Valle SM, Vischioni B, Vitolo V, and Sarti A. Inter-fractional monitoring of ^{12}C ions treatments: results from a clinical trial at the CNAO facility. Sci. Rep. 2020; **10**(1) 20735. DOI: 10.1038/s41598-020-77843-z

55. Ammazzalorso F, Graef S, Weber U, Wittig A, Engenhart-Cabillic R, and Jelen U. Dosimetric consequences of intrafraction prostate motion in scanned ion beam radiotherapy. Radiother. Oncol. 2014; **112**(1) 100–5. DOI: 10.1016/j.radonc.2014.03.022

56. Kelleter L, Marek L, Echner G, Ochoa-Parra P, Winter M, Harrabi S, Jakubek J, Jäkel O, Debus J, and Martisikova M. An in-vivo treatment monitoring system for ion-beam radiotherapy based on 28 Timepix3 detectors. Sci. Rep. 2024; **14**(1) 15452. DOI: 10.1038/s41598-024-66266-9

57. Jäkel O, Jacob C, Schardt D, Karger CP, and Hartmann GH. Relation between carbon ion ranges and x-ray CT numbers. Med. Phys. 2001; **28**(4) 701–3. DOI: 10.1118/1.1357455

58. Muraro S, Battistoni G, Collamati F, De Lucia E, Faccini R, Ferroni F, Fiore S, Frallicciardi P, Marafini M, Mattei I, Morganti S, Paramatti R, Piersanti L, Pinci D, Rucinski A, Russomando A, Sarti A, Sciubba A, Solfaroli-Camillocci E, Toppi M, Traini G, Voena C, and Patera V. Monitoring of Hadrontherapy Treatments by Means of Charged Particle Detection. Front. Oncol. 2016; **6** 177. DOI: 10.3389/fonc.2016.00177

59. Tsujii H. Overview of Carbon-ion Radiotherapy. J. Phys. Conf. Ser. 2017; **777** 012032. DOI: 10.1088/1742-6596/777/1/012032

60. Finck C, Karakaya Y, Reithinger V, Rescigno R, Baudot J, Constanzo J, Juliani D, Krimmer J, Rinaldi I, Rousseau M, Testa E, Vanstalle M, and Ray C. Study for online range monitoring with the interaction vertex imaging method. Phys. Med. Biol. 2017; **62**(24) 9220–39. DOI: 10.1088/1361-6560/aa954e

61. Traini G, Mattei I, Battistoni G, Bisogni MG, De Simoni M, Dong Y, Embriaco A, Fischetti M, Magi M, Mancini-Terracciano C, Marafini M, Mirabelli R, Muraro S, Patera V, Schiavi A, Sciubba A, Solfaroli Camillocci E, Valle SM, and Sarti A. Review and performance of the Dose Profiler, a particle therapy treatments online monitor. Phys. Medica 2019; **65** 84–93. DOI: 10.1016/j.ejmp.2019.07.010

62. Henriquet P, Testa E, Chevallier M, Dauvergne D, Dedes G, Freud N, Krimmer J, Létang JM, Ray C, Richard MH, and Sauli F. Interaction vertex imaging (IVI) for carbon ion therapy monitoring: a feasibility study. Phys. Med. Biol. 2012; **57**(14) 4655–69. DOI: 10.1088/0031-9155/57/14/4655

63. Enghardt W, Crespo P, Fiedler F, Hinz R, Parodi K, Pawelke J, and Pönisch F. Charged hadron tumour therapy monitoring by means of PET. Nucl. Instrum. Meth. A 2004; **525**(1-2) 284–8. DOI: 10.1016/j.nima.2004.03.128

64. Handrack J, Tessonnier T, Chen W, Liebl J, Debus J, Bauer J, and Parodi K. Sensitivity of post treatment positron emission tomography/computed tomography to detect inter-fractional range variations in scanned ion beam therapy. Acta Oncol. 2017; **56**(11) 1451–8. DOI: 10.1080/0284186X.2017.1348628

65. Parodi K and Polf JC. In vivo range verification in particle therapy. Med. Phys. 2018; **45**(11) e1036–e1050. DOI: 10.1002/mp.12960

66. Parodi K, Bortfeld T, and Haberer T. Comparison Between In-Beam and Offline Positron Emission Tomography Imaging of Proton and Carbon Ion Therapeutic Irradiation at Synchrotron- and Cyclotron-Based Facilities. Int. J. Radiat. Oncol. Biol. Phys. 2008; **71**(3) 945–56. DOI: 10.1016/j.ijrobp.2008.02.033

67. Pennazio F, Battistoni G, Bisogni MG, Camarlinghi N, Ferrari A, Ferrero V, Fiorina E, Morrocchi M, Sala P, Sportelli G, Wheadon R, and Cerello P. Carbon ions beam therapy monitoring with the INSIDE in-beam PET. Phys. Med. Biol. 2018; **63**(14) 145018. DOI: 10.1088/1361-6560/aacab8

68. Kraan AC, Susini F, Moglioni M, Battistoni G, Bersani D, Carra P, Cerello P, De Gregorio A, Ferrero V, Fiorina E, Franciosini G, Morrocchi M, Muraro S, Patera V, Pennazio F, Retico A, Rosso V, Sarti A, Schiavi A, Sportelli G, Traini G, Vischioni B, Vitolo V, and Bisogni MG. In-beam PET treatment monitoring of

carbon therapy patients: Results of a clinical trial at CNAO. Phys. Medica 2024; **125** 104493. DOI: 10.1016/j.ejmp.2024.104493

69. Testa E, Bajard M, Chevallier M, Dauvergne D, Le Foulher F, Freud N, Létang J, Poizat J, Ray C, and Testa M. Dose profile monitoring with carbon ions by means of prompt-gamma measurements. Nucl. Instrum. Meth. B 2009; **267**(6) 993–6. DOI: 10.1016/j.nimb.2009.02.031

70. Richard MH, Chevallier M, Dauvergne D, Freud N, Henriquet P, Le Foulher F, Létang JM, Montarou G, Ray C, Roellinghoff F, Testa E, Testa M, and Walenta AH. Design Guidelines for a Double Scattering Compton Camera for Prompt-γ Imaging During Ion Beam Therapy: A Monte Carlo Simulation Study. IEEE T. Nucl. Sci. 2011; **58**(1) 87–94. DOI: 10.1109/TNS.2010.2076303

71. Krimmer J, Dauvergne D, Létang JM, and Testa É. Prompt-gamma monitoring in hadrontherapy: A review. Nucl. Instrum. Meth. A 2018; **878** 58–73. DOI: 10.1016/j.nima.2017.07.063

72. Amaldi U, Hajdas W, Iliescu S, Malakhov N, Samarati J, Sauli F, and Watts D. Advanced Quality Assurance for CNAO. Nucl. Instrum. Meth. A 2010; **617**(1-3) 248–9. DOI: 10.1016/j.nima.2009.06.087

73. Ghesquière-Diérickx L, Schlechter A, Félix-Bautista R, Gehrke T, Echner G, Kelleter L, and Martišíková M. Investigation of Suitable Detection Angles for Carbon-Ion Radiotherapy Monitoring in Depth by Means of Secondary-Ion Tracking. Front. Oncol. 2021; **11** 780221. DOI: 10.3389/fonc.2021.780221

74. Gwosch K, Hartmann B, Jakubek J, Granja C, Soukup P, Jäkel O, and Martišíková M. Non-invasive monitoring of therapeutic carbon ion beams in a homogeneous phantom by tracking of secondary ions. Phys. Med. Biol. 2013; **58**(11) 3755–73. DOI: 10.1088/0031-9155/58/11/3755

75. Félix-Bautista R, Gehrke T, Ghesquière-Diérickx L, Reimold M, Amato C, Turecek D, Jakubek J, Ellerbrock M, and Martišíková M. Experimental verification of a non-invasive method to monitor the lateral pencil beam position in an anthropomorphic phantom for carbon-ion radiotherapy. Phys. Med. Biol. 2019; **64**(17) 175019. DOI: 10.1088/1361-6560/ab2ca3

76. Hymers D, Kasanda E, Bildstein V, Easter J, Richard A, Spyrou A, Höhr C, and Mücher D. Intra- and inter-fraction relative range verification in heavy-ion therapy using filtered interaction vertex imaging. Phys Med Biol 2021; **66**(24) 245022. DOI: 10.1088/1361-6560/ac3b33

77. Elsasser C and the LHCb Silicon Tracker Group. The LHCb Silicon Tracker—Performance & radiation damage. Nucl. Instrum. Meth. A 2013; **730** 13–7. DOI: 10.1016/j.nima.2013.04.009

78. Novak A, Granja C, Sagatova A, Jakubek J, Zatko B, Vondracek V, Andrlik M, Zach V, Polansky S, Rathi A, and Oancea C. Silicon Carbide Timepix3 detector for quantum-imaging detection and spectral tracking of charged particles in wide range of energy and field-of-view. J. Instrum. 2023; **18**(11) C11004. DOI: 10.1088/1748-0221/18/11/C11004

79. Alberigi Quaranta A, Taroni A, and Zanarini G. Plasma time and related delay effects in solid state detectors. Nucl. Instrum. Meth. 1969; **72**(1) 72–6. DOI: 10.1016/0029-554X(69)90267-5

80. Lutz G. Semiconductors. *Semiconductor Radiation Detectors: Device Physics*. 1st ed. Heidelberg: Springer Berlin, 1999 7–38

81. Knoll GF. Semiconductor Diode Detectors. *Radiation Detection and Measurement*. 4th ed. John Wiley & Sons, Inc., 2010 365–413

82. Lutz G. Basic Semiconductor Structures. *Semiconductor Radiation Detectors: Device Physics*. 1st ed. Heidelberg: Springer Berlin, 1999 39–75

83. Rodríguez Rodríguez A and the CBM collaboration. Advancements in the Silicon Tracking System of the CBM experiment: module series production, testing, and operational insights. J. Instrum. 2025; **20**(03) C03020. DOI: 10.1088/1748-0221/20/03/C03020

84. Brenner R, Harr R, Rudge A, Santos D, Straver J, Weilhammer P, Czermak A, Gadomski S, Turala M, Bonvicini V, Kucewicz W, Masciocchi S, Vegni G, Peisert A, Ardelan J, Hrisoho A, Troung K, Couchot F, Colledani C, Dulinski W, Husson D, Lounis A, Mayet N, Schaeffer M, Turchetta R, Smith A, Apsimon R, Seller P, Tyndel M, Aalste M, Hietanen I, Lindgren J, Osterberg K, Orava R, Ronnqvist C, Tuuva T, and Voutilainen M. Measurement of the spatial resolution of double-sided double-metal AC-coupled silicon microstrips detectors. Nucl. Instrum. Meth. A 1993; **326**(1-2) 189–97. DOI: 10.1016/0168-9002(93)90350-Q

85. Caccia M, Evensen L, Hansen TE, Horisberger R, Hubbeling L, Peisert A, Tuuva T, Weilhammer P, and Zalewska A. A Si strip detector with integrated coupling capacitors. Nucl. Instrum. Meth. A 1987; **260**(1) 124–31. DOI: 10.1016/0168-9002(87)90393-7

86. Soisson S, Stein B, May L, Dienhoffer R, Jandel M, Souliotis G, Shetty D, Galanopoulos S, Keksis A, Wuenschel S, Kohley Z, Yennello S, Bullough M, Greenwood N, Walsh S, and Wilburn C. A dual-axis dual-lateral position-sensitive detector for charged particle detection. Nucl. Instrum. Meth. A 2010; **613**(2) 240–4. DOI: 10.1016/j.nima.2009.11.053

87. Ballabriga R, Campbell M, and Llopart X. Asic developments for radiation imaging applications: The medipix and timepix family. Nucl. Instrum. Meth. A 2018; **878** 10–23. DOI: 10.1016/j.nima.2017.07.029

88. Elad E and Sareen R. Low Temperature Characteristics of Ion Implanted Silicon Position Sensitive Detectors. IEEE T. Nucl. Sci. 1974; **21**(1) 75–84. DOI: 10.1109/TNS.1974.4327447

89. Pereira-Lopez X, Ahn S, Ahn DS, Bae S, Cha SM, Hahn KI, Hwang JW, Kim D, Kim MJ, Lee HY, Moon B, and Park C. Development and characterization of new position-sensitive silicon strip detectors. Nucl. Instrum. Meth. B 2023; **541** 134–6. DOI: 10.1016/j.nimb.2023.05.009

90. Wu CE, Ye YL, Jiang DX, Zheng T, Hua H, Li ZH, Li XQ, Ge YC, Zhang GL, Pang DY, Wang J, and Lou JL. The timing performance of a two-dimensional position-sensitive silicon detector. Nucl. Instrum. Meth. A 2005; **555**(1-2) 266–9. DOI: 10.1016/j.nima.2005.09.026

91. Knoll GF. Pulse Processing. *Radiation Detection and Measurement*. 4th ed. John Wiley & Sons, Inc., 2010 595–624

92. Giraud P, Yorke E, Jiang S, Simon L, Rosenzweig K, and Mageras G. Reduction of organ motion effects in IMRT and conformal 3D radiation delivery by using gating and tracking techniques. Cancer Radiother. 2006; **10**(5) 269–82. DOI: 10.1016/j.canrad.2006.05.009

93. Lehnert J, Byszuk A, Emschermann D, Kasinski K, Müller W, Schmidt C, Szczygiel R, and Zabolotny W. GBT based readout in the CBM experiment. J. Instrum. 2017; **12**(02) C02061. DOI: 10.1088/1748-0221/12/02/C02061

94. Heuser J, Murin Y, Schmidt CJ, Soyk D, and Sturm C. Progress with micro-strip sensors for the CBM Silicon Tracking System. CBM Progress Report 2015 2016 22. Available from: https://repository.gsi.de/record/186952

95. Kasinski K, Rodriguez-Rodriguez A, Lehnert J, Zubrzycka W, Szczygiel R, Otfinowski P, Kleczek R, and Schmidt C. Characterization of the STS/MUCH-XYTER2, a 128-channel time and amplitude measurement IC for gas and silicon microstrip sensors. Nucl. Instrum. Meth. A 2018; **908** 225–35. DOI: 10.1016/j.nima.2018.08.076

96. Heuser JM, Bertini O, Eschke J, Lavrik E, Panasenko I, Schmidt CJ, Schmidt HR, Frankenfeld U, Simons C, Schünemann K, Mehta S, Bajdel M, Shiroya M, Wilms A, Al-Turany H, Bailey J, and Neumann J. Start of STS microstrip sensor series production and testing. CBM Progress Report 2019 2020 16–9. DOI: 10.15120/GSI-2020-00904

97. Blank T, Pfistner P, Speck R, Trifonova E, Eisenblätter L, Leyrer B, and Caselle M. Copper based Micro-Cables for STS modules. CBM Progress Report 2019 2020 27–9. DOI: 10.15120/GSI-2020-00904

98. Kasinski K, Kleczek R, and Szczygiel R. Front-end readout electronics considerations for Silicon Tracking System and Muon Chamber. J. Instrum. 2016; **11**(02) C02024. DOI: 10.1088/1748-0221/11/02/C02024

99. Lehnert J, Müller WFJ, and Schmidt CJ. The GBT-based readout concept for the silicon tracking system of the CBM experiment. *Photonics Applications in Astronomy, Communications, Industry, and High-Energy Physics Experiments 2015*. Vol. 9662. Wilga, Poland: SPIE, 2015 763–70. DOI: 10.1117/12.2205623

100. Zabołotny W, Byszuk A, Dementev D, Emschermann D, Gumiński M, Kruszewski M, Miedzik P, Poźniak K, Romaniuk R, Schmidt C, and Shitenkov M. GBTX emulator for development and special versions of GBT-based readout chains. J. Instrum. 2021; **16**(12) C12022. DOI: 10.1088/1748-0221/16/12/C12022

101. Kasinski K, Zubrzycka W, and Szczygiel R. Microstrip and gas electron multiplier readout ASIC for physics experiment at FAIR. *2017 MIXDES - 24th International Conference "Mixed Design of Integrated Circuits and Systems"*. Bydgiszcz, Poland, 2017 285–9. DOI: 10.23919/MIXDES.2017.8005217

102. Zabołotny W, Byszuk A, Gumiński M, Kasprowicz G, Kruszewski M, Poźniak K, Romaniuk R, Emschermann D, and Schmidt C. GBTX Emulation for BM@N/MPD Data Acquisition Systems. Acta Phys. Pol. B Proc. Suppl. 2021; **14**(3) 555–8. DOI: 10.5506/APhysPolBSupp.14.555

103. Otfinowski P, Grybos P, Szczygiel R, and Kasinski K. Offset correction system for 128-channel self-triggering readout chip with in-channel 5-bit energy measurement functionality. Nucl. Instrum. Meth. A 2015; **780** 114–8. DOI: 10.1016/j.nima.2015.01.048

104. Schoemers C, Feldmeier E, Galonska M, Horn JT, Peters A, and Haberer T. First Tests of a Re-accelerated Beam at Heidelberg Ion-Beam Therapy Centre (HIT). *Proceedings of IPAC2017*. Copenhagen, Denmark: JACoW Publishing, Geneva, Switzerland, 2017 4647–9. DOI: 10.18429/JACoW-IPAC2017-THPVA083

105. Tinganelli W, Sokol O, Quartieri M, Puspitasari A, Dokic I, Abdollahi A, Durante M, Haberer T, Debus J, Boscolo D, Voss B, Brons S, Schuy C, Horst F, and Weber U. Ultra-High Dose Rate (FLASH) Carbon Ion Irradiation: Dosimetry and First Cell Experiments. Int. J. Radiat. Oncol. Biol. Phys. 2022; **112**(4) 1012–22. DOI: 10.1016/j.ijrobp.2021.11.020

106. Piersanti L, Bellini F, Bini F, Collamati F, De Lucia E, Durante M, Faccini R, Ferroni F, Fiore S, Iarocci E, La Tessa C, Marafini M, Mattei I, Patera V, Ortega PG, Sarti A, Schuy C, Sciubba A, Vanstalle M, and Voena C. Measurement of charged particle yields from PMMA irradiated by a 220 MeV/u ^{12}C beam. Phys. Med. Biol. 2014; **59**(7) 1857–72. DOI: 10.1088/0031-9155/59/7/1857

8 List of Figures